

DISSERTAÇÃO DE MESTRADO Nº 1205

**A DGTD METHOD USING CURVED ELEMENTS TO SOLVE  
ELECTROMAGNETIC SCATTERING PROBLEMS**

**Marlon Jesus Lizarazo Urbina**

DATA DA DEFESA: 21/10/2020

**Universidade Federal de Minas Gerais**

**Escola de Engenharia**

**Programa de Pós-Graduação em Engenharia Elétrica**

**A DGTD METHOD USING CURVED ELEMENTS TO SOLVE  
ELECTROMAGNETIC SCATTERING PROBLEMS**

Marlon Jesus Lizarazo Urbina

Dissertação de Mestrado submetida à Banca Examinadora designada pelo Colegiado do Programa de Pós-Graduação em Engenharia Elétrica da Escola de Engenharia da Universidade Federal de Minas Gerais, como requisito para obtenção do Título de Mestre em Engenharia Elétrica.

Orientador: Elson José da Silva

Belo Horizonte - MG

Outubro de 2020

U73d

Urbina, Marlon Jesus Lizarazo.

A DGTD method using curved elements to solve electromagnetic scattering problems [recurso eletrônico] / Marlon Jesus Lizarazo Urbina. – 2020.

1 recurso online (xv, 58 f. : il., color.) : pdf.

Orientador: Elson Jose da Silva.

Dissertação (mestrado) Universidade Federal de Minas Gerais, Escola de Engenharia.

Bibliografia: f. 52-58.

Exigências do sistema: Adobe Acrobat Reader.

1. Engenharia elétrica - Teses. 2. Galerkin, Métodos de - Teses. 3. Espalhamento - Teses. I. Silva, Elson José da. II. Universidade Federal de Minas Gerais. Escola de Engenharia. III. Título.

CDU: 621.3(043)

**"A Dgtd Method Using Curved Elements To Solve  
Electromagnetic Scattering Problems"**

**Marlon Jesus Lizarazo Urbina**

Dissertação de Mestrado submetida à Banca Examinadora designada pelo Colegiado do Programa de Pós-Graduação em Engenharia Elétrica da Escola de Engenharia da Universidade Federal de Minas Gerais, como requisito para obtenção do grau de Mestre em Engenharia Elétrica.

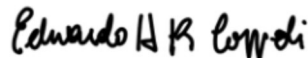
Aprovada em 21 de outubro de 2020.

Por:



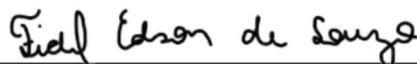
---

**Prof. Dr. Elson José da Silva**  
DEE (UFMG) - Orientador



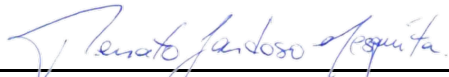
---

**Prof. Dr. Eduardo Henrique da Rocha Coppoli**  
Eng. Elétrica (CEFET-MG)



---

**Prof. Dr. Fidel Edson de Souza**  
Engenharia (UFVJM Campus de Janaúba)



---

**Prof. Dr. Renato Cardoso Mesquita**  
DEE (UFMG)

# Agradecimientos

Este trabajo está dedicado a todas y cada una de las personas que han estado ahí, no solo brindándome su apoyo, si no también soportándome durante este proceso que siempre recordaré como una de las mejores experiencias de mi vida.

En primer lugar, me gustaría agradecer a mi madre, a mi padre y a mi hermanito por haber estado conmigo incondicionalmente en cada uno de los momentos difíciles de mi vida.

También me gustaría agradecerle al profesor Elson por brindarme la oportunidad de trabajar con él y sobre todo por la paciencia que tuvo al compartirme parte de su conocimiento durante todo este proceso.

Quiero agradecer también a mis abuelos, tíos, primos... por el cariño y el apoyo que siempre me brindaron desde la distancia.

Además, quiero agradecerle a Jose Olger (el patrón) por ayudarme en los primeros momentos cuando llegué a brasil y sobre todo por su amistad incondicional.

Y por último pero no menos importante, me gustaría agradecerle a todos mis amigos: Andres, Luigy, Maria y Diego. ¡Gracias por tan bellos y buenos momentos muchachos!

# Resumo

O aumento do uso de métodos numéricos para resolver problemas de espalhamento eletromagnético impulsiona o estudo de uma discretização espacial ótima para obter uma solução mais precisa. Nesta dissertação, o uso de elementos curvos (CEs) no método galerkin descontínuo no domínio do tempo (DGTD) é apresentado como uma alternativa aos elementos retos (SSE). Como pode ser visto ao longo deste trabalho, os CEs apresentam muitas vantagens em problemas que envolvem contornos curvos pois esses contornos são representados com precisão, evitando o uso de pequenos SSE e, conseqüentemente, diminuindo o número de graus de liberdade (DOF).

Inicialmente, apresentamos o método clássico DGTD com SSE. Isso foi essencial porque nesta parte são mencionadas muitas das características importantes do método como: o uso do fluxo numérico para garantir a conectividade entre os elementos, a base polinomial ortonormal usada para construir a forma semidiscretizada e o método de Runge Kutta usado para a integração do tempo. Em seguida, é explicado o passo a passo das modificações que devem ser feitas para implementar os elementos curvos. O processo de construção dos CEs pode ser dividido em três partes: a primeira é identificar os elementos que são interceptados pela fronteira curva, a segunda é reposicionar os nós da face curva exatamente na fronteira curva e a terceira, aplicar a deformação sobre os nós internos dos CEs e atualizar as localizações dos nós. Além disso, as integrais de funções não polinomiais devem ser levadas em consideração já que o jacobiano de cada CE não é constante.

Para validar esta formulação, problemas de espalhamento em 2D foram resolvidos. Os resultados mostraram que o erro global diminui quando os CEs são usados. Além disso, a taxa de convergência foi maior para os CEs do que para os SSE. Adicionalmente, foi apresentado o uso de CEs para resolver problemas mais complexos onde a quantidade de CEs aumenta muito. Novamente, o esquema dos CEs teve uma solução melhor do que com os SSE junto com uma diminuição do número de elementos e de DOF.

**Palavras-chave:** DGTD, elementos curvos, fronteiras curvas, problemas de espalhamento.

# Abstract

The increase in the use of numerical methods to solve electromagnetic scattering problems drives the study of an optimal spatial discretization to obtain a more accurate solution. In this dissertation, the use of curved elements (CE) in the Discontinuous Galerkin Time Domain (DGTD) method is presented as an alternative to common straight side elements (SSE). As can be seen throughout this work, CEs have many advantages in problems involving curved contours because these contours are represented accurately avoiding the use of small SSE and consequently, decreasing the number of nodes on the computational domain, also called degrees of freedom (DOF).

Initially, the classical DGTD method with SSE is explained. This is essential because in this part are mentioned most of important characteristics of the method as: the use of the numerical flux to guarantee the connectivity between elements, the orthonormal polynomial basis used to build the semi-discretized form and the Runge Kutta method used for the time integration. Then, it is explained step by step the modifications which must be done to make the curved elements. The process to build the CEs can be divided into three parts: the first one is to identify the elements which are intersected by the curved boundary, the second one is to relocate the nodes of the curved face exactly onto the curved boundary and third, to apply the deformation over the internal nodes of the CEs and update the volume nodes locations. Moreover, the integrals of non-polynomials functions must be taken into consideration due to the jacobian of each curved element is non-constant.

In order to validate this formulation, 2D scattering problems were solved. Results showed that the global error decreases when the CEs are used. Moreover, the convergence rate was higher for the CEs than the SSE. Additionally, the use of CEs to solve more complex problems where the amount of CEs increases a lot was presented. Again, the CEs scheme showed a more accurate solution than the SSE with a decrease of number of elements and DOF.

**Keywords:** DGTD, curved elements, curved boundaries, scattering problems.

# List of Figures

|      |  |    |
|------|--|----|
| 2.1  | Neighbor elements with the same edge $e$ . . . . .   | 12 |
| 2.2  | Nodal distribution for $N = 4$ and 6. . . . .  | 18 |
| 3.1  | Two possible cases of boundary triangle $K$ . (a) Convex case, (b) Concave case. . . . .   | 23 |
| 3.2  | CE with neighbor elements . . . . .  | 24 |
| 3.3  | (a) Straight side element. (b) Nodes deformed on the face curved. (c) Final nodes distribution in the CE . . . . .   | 27 |
| 3.4  | Straight side element near to curved boundary . . . . .  | 27 |
| 4.1  | Concentric PEC cylinders resonator. . . . .  | 31 |
| 4.2  | Triangular meshes and component $E_z$ of the solution for the concentric PEC cylinders resonator at time $t=0.333\text{ns}$ , using (a) straight side and (b) curved elements. . . . . | 33 |
| 4.3  | P-convergence for the concentric PEC cylinders resonator, using straight side and curved elements. . . . .   | 34 |
| 4.4  | Uniform plane wave illuminating a PEC circular cylinder. . . . .   | 35 |
| 4.5  | Scattered field by a PEC circular cylinder using (a) straight side and (b) curved elements for the mesh 1. . . . .   | 36 |
| 4.6  | P-convergence for the scattered field by a PEC circular cylinder problem, using straight side and curved elements. . . . .   | 37 |
| 4.7  | x-wise 1D distribution of the solution of the scattered field by a PEC circular cylinder for straight side and curved elements. . . . .  | 37 |
| 4.8  | Uniform plane wave illuminating a dielectric circular cylinder. . . . .  | 39 |
| 4.9  | Scattered field by a dielectric circular cylinder using (a) straight side and (b) curved elements for the mesh 1. . . . .  | 40 |
| 4.10 | P-convergence for the scattered field by a dielectric circular cylinder problem, using straight side and curved elements. . . . .  | 40 |



|      |  |    |
|------|--|----|
| 4.11 | x-wise 1D distribution of the solution of the scattered field by a dielectric circular cylinder for straight side and curved elements at time $t=26.67\text{ns}$ . . . . .                                       | 41 |
| 4.12 | Uniform plane wave illuminating a PEC coated circular cylinder. . . . .  | 42 |
| 4.13 | x-wise 1D distribution of the solution of the scattered field by a PEC coated circular cylinder for straight side and curved elements at time $t=26.67\text{ns}$ . . . . .                                       | 43 |
| 4.14 | Total and Scattered field by a PEC coated circular cylinder at time $t=26.67\text{ns}$ , using straight side and curved elements . . . . .   | 43 |
| 4.15 | Photonic crystal structure. . . . .  | 45 |
| 4.16 | L-shaped photonic crystal guide. . . . .   | 45 |
| 4.17 | L-shaped photonic crystal guide, (a) computational domain represented by a refined triangular mesh, (b) Component $E_z$ of solution, (c) dielectric scatter represented by small straight side elements. . . . . | 46 |
| 4.18 | L-shaped photonic crystal guide, (a) computational domain represented by a triangular mesh, (b) Component $E_z$ of solution, (c) dielectric scatter represented by curved elements. . . . .                      | 47 |
| 4.19 | FFT of the signals propagated inside the waveguide. . . . .  | 48 |

# List of Tables

|      |   |    |
|------|---|----|
| 1.1  | Comparison of numerical methods [i.e., finite difference methods (FDTD), finite volume methods (FVTD), finite element methods (FEMTD) and discontinuous galerkin finite element method (DGTD-FEM)]. The symbol * reflects that the method would have this feature if some modifications are made. . . . . | 2  |
| 2.1  | Parameters of centered, upwind and penalized numerical fluxes. . . . .  | 13 |
| 4.1  | Characteristics of grids used for the concentric PEC cylinders resonator. . . . .   | 32 |
| 4.2  | $L^2$ errors at time $t=0.333\text{ns}$ and convergence rates for h-refinement using the general DGTD into the concentric PEC cylinders resonator problem. . . . .  | 33 |
| 4.3  | $L^2$ errors at time $t=0.333\text{ns}$ and convergence rates for h-refinement using the modified DGTD with CE into the concentric PEC cylinders resonator problem. . . . .   | 33 |
| 4.4  | Characteristics of the grids used for the scattering by a PEC circular cylinder. . . . .  | 35 |
| 4.5  | $L^2$ errors at time $t=26.67\text{ns}$ and convergence rates for h-refinement using the general DGTD into the scattering by a PEC circular cylinder problem. . . . .   | 36 |
| 4.6  | $L^2$ errors at time $t=26.67\text{ns}$ and convergence rates for h-refinement using the modified DGTD with CE into the scattering by a PEC circular cylinder problem. . . . .  | 36 |
| 4.7  | Grids used for the scattering by a dielectric circular cylinder. . . . .  | 38 |
| 4.8  | $L^2$ errors at time $t=26.67\text{ns}$ and convergence rates for h-refinement using the general DGTD into the scattering by a dielectric circular cylinder problem. . . . .  | 39 |
| 4.9  | $L^2$ errors at time $t=26.67\text{ns}$ and convergence rates for h-refinement using the modified DGTD with CE into the scattering by a dielectric circular cylinder problem. . . . .   | 39 |
| 4.10 | Characteristics of grids used for the scattering by a PEC coated circular cylinder. . . . .   | 42 |
| 4.11 | Meshes used to represent the L-shaped photonic guide. . . . .   | 46 |

|   |    |
|---|----|
| 4.12 Central frequencies for each pulses. . . . . | 48 |
|---|----|

# List of Symbols

|                    |  |
|--------------------|--|
| <b>a</b>           | Lattice constant in a photonic crystal                   |
| <b>B</b>           | Magnetic flux intensity ( <i>coulomb/m<sup>2</sup></i> ) |
| <i>c</i>           | Velocity of light  |
| <i>C</i>           | Courant–Friedrichs–Lewy (CFL) constant                   |
| <b>d</b>           | Waveguide length in a photonic crystal                   |
| <b>D</b>           | Electric flux intensity ( <i>weber/m<sup>2</sup></i> )   |
| $\mathcal{D}_r$    | Differentiation matrix in relation to r                  |
| $\mathcal{D}_s$    | Differentiation matrix in relation to s                  |
| <b>E</b>           | Electric field intensity ( <i>V/m</i> )                  |
| $E_z$              | Component z of electric field ( <i>V/m</i> )             |
| <b>F*</b>          | Numerical flux   |
| <b>H</b>           | Magnetic field intensity ( <i>A/m</i> )                  |
| $H_z$              | Component z of magnetic field ( <i>A/m</i> )             |
| <b>J</b>           | Electric current density ( <i>A/m<sup>2</sup></i> )      |
| $\mathcal{M}$      | Mass matrix  |
| <b>S</b>           | Stiffness matrix   |
| <i>V</i>           | Vandermonde matrix                                       |
| $V_r$              | Derivative of the Vandermonde matrix in relation to r    |
| $V_s$              | Derivative of the Vandermonde matrix in relation to s    |
| <i>Y</i>           | Conductance of the media                                 |
| <i>Z</i>           | Impedance of the media                                   |
| $e_r$              | error calculate with the $L^2$ norm                      |
| $\varepsilon_0$    | Electric permittivity in the vacuum ( <i>F/m</i> )       |
| $\mu_0$            | Magnetic permeability in the air ( <i>H/m</i> )          |
| $\varepsilon_r$    | Relative electric permittivity in the media              |
| $\mu_r$            | Relative magnetic permeability of media                  |
| +                  | Represents the neighbor element                          |
| –                  | Represents the local element                             |
| $\hat{\mathbf{n}}$ | represents the outwardly directed normal vector          |
| $h^e$              | The length of the triangle edge                          |
| $\Delta t$         | Time step  |
| $\Delta h_{ki}$    | Minimum distance between two nodes in a element          |
| $\eta$             | Refractive index   |

# List of Abbreviations

|         |   |
|---------|---|
| CE      | Curved Element  |
| FD      | Frequency Domain  |
| FDM     | Finite Difference Method  |
| FEM     | Finite Element Method   |
| FFT     | Fast Fourier Transform  |
| FVM     | Finite Volume Method  |
| DG      | Discontinuous Galerkin  |
| DG-FEM  | Discontinuous Galerkin Finite Element Method                    |
| DOF     | Degrees of Freedom  |
| DGTD    | Discontinuous Galerkin Time Domain                              |
| LP2     | Leap Frog Algorithm   |
| LSER4   | Low Storage Five-stage Fourth-order Explicit Runge Kutta Method |
| LTS     | Local Time Stepping   |
| mCSSPMS | Multiclass Linear Multistep Strong Stability Preserving Method  |
| MKS     | Meter, Kilogram and Second                                      |
| PBG     | Photonic Band Gap   |
| PDE     | Partial Differential Equations                                  |
| PEC     | Perfectly Electric Conducting                                   |
| PhC     | Photonic Crystal  |
| PMC     | Perfectly Magnetic Conducting                                   |
| SMA     | Silver-Muller Absorbing   |
| TD      | Time Domain   |
| TE      | Transverse Electric   |
| TM      | Transverse Magnetic   |

# Contents

|  |             |
|--|-------------|
| <b>Agradecimientos</b>                                   | <b>v</b>    |
| <b>Resumo</b>  | <b>vi</b>   |
| <b>Abstract</b>  | <b>vii</b>  |
| <b>List of Figures</b>                                   | <b>viii</b> |
| <b>List of Tables</b>                                    | <b>x</b>    |
| <b>List of Symbols</b>                                   | <b>xii</b>  |
| <b>List of Abbreviations</b>                             | <b>xiii</b> |
| <b>1 Introduction</b>                                    | <b>1</b>    |
| 1.1 Overview of numerical methods in TD . . . . .        | 2           |
| 1.1.1 Finite Differences in Time Domain (FDTD) . . . . . | 2           |
| 1.1.2 Finite Volume Methods (FVTD) . . . . .             | 3           |
| 1.1.3 Finite Element Methods (FEMTD) . . . . .           | 3           |
| 1.1.4 Discontinuous Galerkin Methods (DGTD) . . . . .    | 4           |
| 1.2 Some applications of DGTD . . . . .                  | 4           |
| 1.2.1 Waveguides . . . . .                               | 4           |
| 1.2.2 Antennas . . . . .                                 | 4           |
| 1.2.3 Photonic Crystals (PhC) . . . . .                  | 5           |
| 1.3 Objectives and Contributions . . . . .               | 5           |
| 1.4 Survey of chapters . . . . .                         | 6           |
| <b>2 The Discontinuous Galerkin Time Domain Method</b>   | <b>7</b>    |
| 2.1 Maxwell's equations . . . . .                        | 7           |
| 2.2 Maxwell's equations in conservation form . . . . .   | 10          |

|          |  |           |
|----------|--|-----------|
| 2.2.1    | TM mode . . . . .  | 10        |
| 2.3      | The Galerkin method . . . . .  | 11        |
| 2.3.1    | Numerical flux . . . . .   | 12        |
| 2.3.2    | Boundary conditions . . . . .  | 14        |
| 2.4      | Semi-discretized form . . . . .  | 16        |
| 2.4.1    | Nodal distribution . . . . .   | 17        |
| 2.4.2    | Mass and stiffness matrices . . . . .  | 17        |
| 2.4.3    | Flux discretization . . . . .  | 19        |
| 2.5      | Low-Storage Explicit Runge Kutta fourth order method for time inte-<br>gration . . . . . | 20        |
| 2.5.1    | Conditional stability and time step . . . . .  | 21        |
| <b>3</b> | <b>Curved Elements</b>   | <b>22</b> |
| 3.1      | Strong variational form for the CE . . . . .   | 22        |
| 3.1.1    | Convex case . . . . .  | 24        |
| 3.1.2    | Concave case . . . . .   | 25        |
| 3.2      | Forming curved elements . . . . .  | 26        |
| 3.3      | Operators on curved elements . . . . .   | 28        |
| <b>4</b> | <b>Results and Discussion</b>  | <b>30</b> |
| 4.1      | Concentric PEC cylinders resonator . . . . .   | 31        |
| 4.2      | Scattering by a PEC circular cylinder . . . . .  | 34        |
| 4.3      | Scattering by a dielectric circular cylinder . . . . .                                   | 38        |
| 4.4      | Scattering by a PEC coated circular cylinder . . . . .                                   | 41        |
| 4.5      | L-shaped photonic crystal guide . . . . .  | 44        |
| <b>5</b> | <b>Conclusions</b>   | <b>50</b> |
| 5.1      | Futures works . . . . .  | 51        |
|          | <b>Bibliography</b>  | <b>52</b> |

# Chapter 1

## Introduction

Discontinuous Galerkin Time Domain (DGTD) method is a very powerful numerical technique for solving Partial Differential Equations (PDE). This method has a lot of possibilities to be implemented since it can be easily discretized both in space domain and time domain. It has successfully been used to solve a lot of differential equations in some areas as: Aerodynamics [Silveira et al., 2015], Nano-optical problems [Hille et al., 2010], Elastodynamics [Petersen et al., 2009; Dumbser et al., 2007], and Quantum mechanics [Xu and Shu, 2005].

In the discontinuous Galerkin (DG) spatial discretization, we have the advantage of using unstructured meshes with high order finite elements. This allows an accurate discretization of some complex geometries using elements with different sizes (*h* – *adaptivity*), and a high order convergence of the solution can be obtained depending on the order of basis functions (*p* – *adaptivity*). Furthermore, DG method can be applied in both the time domain (TD) and the frequency domain (FD). However, working in TD offers several benefits in electromagnetic problems, such as transient field effect of an arbitrary time signal excitation (e.g. scatter problems, ultra-wideband antennas, photonic crystal guides).

All works mentioned above have focused exclusively on the simplest cases in which all boundaries are approximated by straight side element. This is a good option when there are not complex boundaries, but in some cases a linear approximation is not enough [Bassi and Rebay, 1997]. Therefore, the accurate representation of the domain and its boundary has been studied by many authors [Krivodonova and Berger, 2006; Luo et al., 2001; Van der Vegt and Ven, 2001] among others. In fact, it is necessary to take the effect of the boundary curvature into consideration in order to have a consistent boundary discretization. There are a lot of works published on the DG methods for time domain Maxwell's equation. However, most of them use straight side elements to



approximate the curved geometries and do not show any study of the induced error caused by the inaccurate representation of these surfaces [Cohen et al., 2006; Fahs, 2009a,b]. Thus, in this work the use of isoparametric curvilinear elements (CE) will be investigated in order to decrease the induced error caused by the representation of curved surfaces with straight side elements. Next, a full review of the state of the art is presented including the most used numerical methods and both the advantages and disadvantages of them in comparison with the DG method. Furthermore, this Section was divided into two parts: The first one shows an overview of TD numerical methods and the second one shows some applications in engineering problems using DGTD method.

## 1.1 Overview of numerical methods in TD

There are many TD numerical methods to solve Maxwell's equations. However, each one has different features in comparison with the others. In table 1.1 presented in [Angulo, 2014], it can be seen a summary of the most widely used numerical methods for modeling electromagnetics problems..

Table 1.1: Comparison of numerical methods [i.e., finite difference methods (FDTD), finite volume methods (FVTD), finite element methods (FEMTD) and discontinuous galerkin finite element method (DGTD-FEM)]. The symbol \* reflects that the method would have this feature if some modifications are made.

|                            | FDTD | FVTD | FEMTD | DGTD |
|----------------------------|------|------|-------|------|
| Complex geometries         | No   | Yes  | Yes   | Yes  |
| Explicit semidiscrete form | Yes  | Yes  | No    | Yes  |
| Conservation laws          | Yes  | Yes  | Yes*  | Yes  |
| Spurious modes             | No   | No   | No*   | No*  |
| $h$ adaptivity             | Yes  | Yes  | Yes   | Yes  |
| $p$ adaptivity             | No   | No   | Yes   | Yes  |
| Local time stepping (LTS)  | No   | Yes  | Yes   | Yes  |

### 1.1.1 Finite Differences in Time Domain (FDTD)

FDTD was presented for the first time in 1996 [Yee, 1966] as a scheme to solve Maxwell's equations in isotropic media, it has been extensively developed since then in computational electromagnetics. The classical FDTD method uses a second order finite centered approximations for space and time derivatives in Maxwell's curl equations. In this

technique both the electric as magnetic fields are calculated in a rectilinear cartesian grid, using the second order leap frog (LF2) algorithm. As a result, a second order convergence scheme is obtained with respect to spatial and temporal discretization.

The two main claimed advantages of FDTD are the free spurious solutions and its computational efficiency. However, space discretization based on a rectilinear grid implies a high difficulty to represent complex geometries. Some techniques can be found in the literature that mitigate this limitation, for example: geometrically conformal [Dey and Mittra, 1997] or subgridding [Sarris, 2007]. Additionally, higher order techniques can be implemented for the FDTD algorithm, but these formulations require more effort, reducing their computational efficiency [Young, 2001; Georgakopoulos et al., 2002; Hwang, 2003].

### 1.1.2 Finite Volume Methods (FVTD)

The FVTD was introduced as an alternative to FDTD with the objective of eliminating the restrictions of geometric discretization, avoiding the rectilinear cartesian grid discretization. However, despite improving the spatial discretization of the domain, the FVTD has order of convergence equal to one [Bommaraju et al., 2009] which is quite low. The most known formulation of FVTD is based on tetrahedral elements for the Maxwell's curl equation [Baumann et al., 2008; Sankaran et al., 2006; Fumeaux et al., 2004]. FVTD uses the LF2 algorithm for time discretization as in the FDTD. Furthermore, the time step depends on the shape of the elements which implies a higher restriction than for the FDTD method. One solution to alleviate this restricted time stepping is to use local time step (LTS) techniques [Fumeaux et al., 2004]. Finally, due to the similar features with the DGTD it can be said that FVTD is a Zero-order DGTD method.

### 1.1.3 Finite Element Methods (FEMTD)

There are many schemes of time domain FEM based on the hyperbolic system of curl equations (Ampere's and Faraday's laws) or Maxwell's curl-curl equation [Lee et al., 1997]. Nevertheless, the most common in the literature is the second order vector wave curl-curl equation, generally implemented in FD, but it can also be solved in TD needing just the computation of a single field (electric or magnetic) [Lynch and Paulsen, 1990; Lee, 1994; Lee and Sacks, 1995; Gedney and Navsariwala, 1995]. In this case, a global linear system of equations at each time step has to be solved generating a considerable computational cost. In addition, other alternatives to the single field

scheme can be found in the literature [Rieben et al., 2005; He and Teixeira, 2006, 2007; Donderici and Teixeira, 2008a,b]. These formulations have some advantages, such as avoiding spurious solutions, using different expansion functions. To eliminate the need of saving previous states in memory, these schemes allow the use of a LF2 time integration.

#### 1.1.4 Discontinuous Galerkin Methods (DGTD)

The DGTD can be considered a member of the FEMDT family. This method is introduced with the aim of relaxing the tangential continuity condition. In this case, the continuity is imposed via numerical fluxes in order to connect the solution among neighbor elements. In comparison with the others FEM in TD, the main advantage is that the linear system to be solved is block-diagonal and only requires a single inversion of  $K$  square matrices of  $N \times N$  elements ( $K$  is the number of elements and  $N$  the number of basis functions per element). A lot of works using the DGTD method can be found in the literature. Therefore, in order to show the relevance of this method, the following subsection presents some particular interest areas.

## 1.2 Some applications of DGTD

### 1.2.1 Waveguides

In some cases, the simulation of waveguides needs the modeling of complex geometries where DGTD offers an excellent approach. Also, DGTD is an excellent choice to calculate the resonant frequencies, because the TD simulation allows us to estimate them in a single run. One important characteristic of waveguides is that they are structures where the absence of spurious modes is obligatory [Alvarez et al., 2012]. However, as it will be presented in chapter 2, DGTD has the possibility of choosing different numerical fluxes to avoid spurious modes.

### 1.2.2 Antennas

In the simulation of wideband antennas it is very important to model their geometrical details accurately, especially in critical zones such as feeding ports. These problems have been solved with FDTD and FEMTD methods. However, a very refined spatial discretization in the whole domain is necessary in FDTD, increasing the computational cost. On the other hand, these problems generate in FEMTD a very big global matrix

that has to be solved at each time step, producing a high computational cost. The DGTD with LTS techniques can be used as alternative [Alvarez et al., 2015].

### 1.2.3 Photonic Crystals (PhC)

Photonic crystals, also known as photonic band gap (PBG) materials, can mold the flow of light in a controlled way. They are periodic arrays of dielectric materials that open band spaces for electromagnetic waves, that is, frequency ranges where the propagation of photons is prohibited. These structures can be modeled using FDTD methods [Mekis et al., 1999]. However, the cell size must be decreased to approximate the circular dielectric scatters which implies a significant increase in computational cost in terms of storage memory and execution time. An interesting solution of a L-Shaped photonic crystal using DGTD and applying a multiclass linear multistep strong stability preserving method (mC-SSPMS) is shown in [de Souza et al., 2019]. Nevertheless, in that work the author uses an unstructured mesh with an h-refinement to represent each dielectric scatter accurately, increasing the computational effort. In this work our aim is to use the CE to model each scatter, decreasing the number of elements necessary to approximate each of them and consequently, decreasing the computational effort.

## 1.3 Objectives and Contributions

The main objective of this work is to implement the DGTD method with CE to represent accurately curved surfaces in order to reduce computational effort and improve accuracy in simulations of 2D electromagnetic scattering problems. In order to achieve this goal, the following steps were carried out:

- To implement the DGTD general formulation with the straight side elements.
- To make the necessary modifications over the DGTD general to build the scheme with CE.
- To define adequate 2D electromagnetic problems where the implementation of the CE presents advantages over the DGTD general.
- To validate the implemented formulation comparing with analytical solutions or verified numerical solutions.

This work presents a significant contribution because represents an alternative for the common numerical methods in the spatial discretization of curved geometries, improving the accuracy of the approximation. Besides, the implementation of curved elements minimizes the number of elements required in the mesh, allowing the use of a minor time step. Partial results of this work were accepted in The 19th Biennial IEEE Conference on Electromagnetic Field Computation (CEFC 2020).

## 1.4 Survey of chapters

This text is organized as follows: Chapter 2 presents step by step the DGTD general formulation and Chapter 3 shows the necessary modifications to use the CEs. Next, the results for different 2D electromagnetic problems are presented and discussed in Chapter 4. Finally, Chapter 5 shows the conclusions of the work and final considerations.

## Chapter 2

# The Discontinuous Galerkin Time Domain Method

DGTD was first proposed in the 1970s by [Reed and Hill, 1973] to solve the linear neutron transport equation. Moreover in 1974 [Lesaint and Raviart, 1974] proposed for the first time a mathematical formulation for this method solving the linear neutron transport equation. In the last years some DGTD versions to solve Maxwell's equation has been proposed, one of the most popular and efficient was proposed in 2002 by [Hesthaven and Warburton, 2002]. This chapter explains the modeling of the electromagnetic propagation using the DGTD method in non-dispersive dielectric media. The most important characteristic of DGTD is that electromagnetic fields can have discontinuous components across the boundary between two neighboring elements, Therefore, to guarantee the coupling among the elements a numerical flux [Hesthaven and Warburton, 2007] is introduced as a penalty term on the basis of a conservation law. This implies two important things, first, the DG method becomes adequate for explicit time stepping and second, the problem end up as an ordinary time-dependent differential equation that can be solved through integration using for example the Runge-Kutta method [Cockburn et al., 2000].

### 2.1 Maxwell's equations

Considering Maxwell's curl equations for lossless isotropic media into:

$$\begin{aligned}\nabla \times \mathbf{E} &= -\frac{\partial \mathbf{B}}{\partial t} \\ \nabla \times \mathbf{H} &= \frac{\partial \mathbf{D}}{\partial t} + \mathbf{J}\end{aligned}\tag{2.1}$$

where  $\mathbf{E}$  and  $\mathbf{H}$  are the electric and magnetic field intensities, respectively.  $\mathbf{D}$  and  $\mathbf{B}$  are the electric and magnetic flux densities.  $\mathbf{D}$  is also called the electric displacement, and  $\mathbf{B}$ , the magnetic induction.

The electric and magnetic flux densities  $\mathbf{D}$ ,  $\mathbf{B}$  are related to the field intensities  $\mathbf{E}$ ,  $\mathbf{H}$  by the so-called constitutive relations, whose precise form depends on the material in which the fields exist. In a homogeneous and isotropic medium, they take their form:

$$\begin{aligned}\mathbf{D} &= \varepsilon_0 \varepsilon_r \mathbf{E} \\ \mathbf{B} &= \mu_0 \mu_r \mathbf{H}\end{aligned}\tag{2.2}$$

where  $\varepsilon_0$  are the electric permittivity and  $\mu_0$  the magnetic permeability of vacuum.  $\varepsilon_r$  and  $\mu_r$  are the relative electric permittivity and magnetic permeability of the media, respectively.

Considering a dielectric media  $\mu_r = 1$  without currents  $J = 0$  and substituting Eq. (2.2) in (2.1), we take:

$$\begin{aligned}\nabla \times \mathbf{E} &= -\mu_0 \frac{\partial \mathbf{H}}{\partial t} \\ \nabla \times \mathbf{H} &= \varepsilon \frac{\partial \mathbf{E}}{\partial t}\end{aligned}\tag{2.3}$$

where  $\varepsilon = \varepsilon_0 \varepsilon_r$ .

For each equation, we write the vector components of the curl operators in cartesian coordinates. This yields the following three scalar equations for the Faraday's law:

$$\mu_0 \frac{\partial H_x}{\partial t} = \frac{\partial E_y}{\partial z} - \frac{\partial E_z}{\partial y}\tag{2.4a}$$

$$\mu_0 \frac{\partial H_y}{\partial t} = \frac{\partial E_z}{\partial x} - \frac{\partial E_x}{\partial z}\tag{2.4b}$$

$$\mu_0 \frac{\partial H_z}{\partial t} = \frac{\partial E_x}{\partial y} - \frac{\partial E_y}{\partial x}\tag{2.4c}$$

and the following three scalar equations for the Ampere's law:

$$\varepsilon \frac{\partial E_x}{\partial t} = \frac{\partial H_z}{\partial y} - \frac{\partial H_y}{\partial z}\tag{2.5a}$$

$$\varepsilon \frac{\partial E_y}{\partial t} = \frac{\partial H_x}{\partial z} - \frac{\partial H_z}{\partial x}\tag{2.5b}$$

$$\varepsilon \frac{\partial E_z}{\partial t} = \frac{\partial H_y}{\partial x} - \frac{\partial H_x}{\partial y}\tag{2.5c}$$

If the system is uniform in one direction, for instance in the  $z$ -direction, then all partial derivatives of the fields with respect to  $z$  must vanish. Under that condition, the set of Eqs. (2.4) and (2.5) reduces to

$$\mu_0 \frac{\partial H_z}{\partial t} = \frac{\partial E_z}{\partial y} - \frac{\partial E_y}{\partial x} \quad (2.6a)$$

$$\mu_0 \frac{\partial H_x}{\partial t} = -\frac{\partial E_z}{\partial y} \quad (2.6b)$$

$$\mu_0 \frac{\partial H_y}{\partial t} = \frac{\partial E_z}{\partial x} \quad (2.6c)$$

and

$$\varepsilon \frac{\partial E_z}{\partial t} = \frac{\partial H_y}{\partial x} - \frac{\partial H_x}{\partial y} \quad (2.7a)$$

$$\varepsilon \frac{\partial E_x}{\partial t} = \frac{\partial H_z}{\partial y} \quad (2.7b)$$

$$\varepsilon \frac{\partial E_y}{\partial t} = -\frac{\partial H_z}{\partial x} \quad (2.7c)$$

Grouping Eqs. (2.6b), (2.6c) and (2.7a) we obtain the called transverse magnetic (TM) mode in two dimensions.

$$\varepsilon \frac{\partial E_z}{\partial t} = \frac{\partial H_y}{\partial x} - \frac{\partial H_x}{\partial y} \quad (2.8)$$

$$\mu_0 \frac{\partial H_x}{\partial t} = -\frac{\partial E_z}{\partial y}$$

$$\mu_0 \frac{\partial H_y}{\partial t} = \frac{\partial E_z}{\partial x}$$

and by the same way, grouping the Eqs. (2.6a), (2.7b) and (2.7c) we get the called transverse electric (TE) mode in two dimensions.

$$\mu_0 \frac{\partial H_z}{\partial t} = \frac{\partial E_z}{\partial y} - \frac{\partial E_y}{\partial x} \quad (2.9)$$

$$\varepsilon \frac{\partial E_x}{\partial t} = \frac{\partial H_z}{\partial y}$$

$$\varepsilon \frac{\partial E_y}{\partial t} = -\frac{\partial H_z}{\partial x}$$

From these two polarizations, we notice that the TE and TM modes do not have any field component in common. Therefore, they can coexist without influencing each



other. It is important to say that for simplicity all results in this work are shown using the TMz mode.

## 2.2 Maxwell's equations in conservation form

A suitable scheme for solving linear systems of hyperbolic problems in complex geometries, exemplified by a scheme for solving Maxwell's equation is:

$$Q \frac{\partial \mathbf{q}}{\partial t} + \nabla \cdot \mathbf{F}(\mathbf{q}) = \mathbf{S} \quad (2.10)$$

where  $Q$  is the material matrix with the media information:

$$Q = \begin{bmatrix} \varepsilon & 0 \\ 0 & \mu \end{bmatrix} \quad (2.11)$$

The state vector  $\mathbf{q}$  is given by:

$$\mathbf{q} = \begin{bmatrix} \mathbf{E} \\ \mathbf{H} \end{bmatrix} \quad (2.12)$$

The flux term  $\mathbf{F}(\mathbf{q})$  can be represented as:

$$\mathbf{F}_i(\mathbf{q}) = \begin{bmatrix} -e_i \times \mathbf{H} \\ e_i \times \mathbf{E} \end{bmatrix} \quad (2.13)$$

With  $\mathbf{F}(\mathbf{q}) = [\mathbf{F}_x(\mathbf{q}), \mathbf{F}_y(\mathbf{q}), \mathbf{F}_z(\mathbf{q})]^T$ . Here  $e_i$  signifies the three cartesian unit vectors  $i = x, y, z$  and  $\mathbf{S} = [\mathbf{S}^E, \mathbf{S}^H]^T$  represents sources, currents and terms introduced by the scattered field formulation. In our case  $\mathbf{S} = 0$ .

### 2.2.1 TM mode

Rewriting the set of Eqs. (2.8) in the conservation form:

$$Q = \begin{pmatrix} \varepsilon & 0 & 0 \\ 0 & \mu_0 & 0 \\ 0 & 0 & \mu_0 \end{pmatrix} ; \mathbf{q} = \begin{bmatrix} \mathbf{E}_z \\ \mathbf{H}_x \\ \mathbf{H}_y \end{bmatrix} ; \nabla \cdot \mathbf{F}(\mathbf{q}) = \begin{pmatrix} -\frac{\partial H_y}{\partial x} + \frac{\partial H_x}{\partial y} \\ \frac{\partial E_z}{\partial y} \\ -\frac{\partial E_z}{\partial x} \end{pmatrix}$$

The flux term can be rewriting as:

$$\begin{aligned}
\nabla \cdot \mathbf{F}(\mathbf{q}) &= -\partial_x \begin{pmatrix} \mathbf{H}_y \\ 0 \\ \mathbf{E}_z \end{pmatrix} + \partial_y \begin{pmatrix} \mathbf{H}_x \\ \mathbf{E}_z \\ 0 \end{pmatrix} \\
&= - \begin{pmatrix} 0 & 0 & 1 \\ 0 & 0 & 0 \\ 1 & 0 & 0 \end{pmatrix} \partial_x \mathbf{q} + \begin{pmatrix} 0 & 1 & 0 \\ 1 & 0 & 0 \\ 0 & 0 & 0 \end{pmatrix} \partial_y \mathbf{q} \\
&= A_x \partial_x \mathbf{q} + A_y \partial_y \mathbf{q}
\end{aligned} \tag{2.15}$$

## 2.3 The Galerkin method

To apply the DG formalism, firstly, we assume that the domain  $\Omega$  is represented by a set of non-overlapping elements,  $K$ , typically tetrahedrons for tridimensional problems or triangles for bidimensional problems, organized in an unstructured manner to fill the computational domain.

$$\Omega = \bigcup_{k=1}^K \Omega_k \tag{2.16}$$

Now, let us consider only a single element of the computational domain. The aim is to find a numerical approximation  $\mathbf{q}_N$  to the correct solution  $\mathbf{q}$  to the Eq. (2.10). For the DG spatial discretization, each element is discontinuous with respect to others. It means that the variational form must be local, therefore, the weak form is obtained by multiplying Eq. (2.10) by a regular test function  $L_j(\mathbf{r}, t)$  which minimizes the residue. Finally, we integrate over the element  $\Omega_k$ .

$$\int_{\Omega_k} \left[ Q \partial_t \mathbf{q}(\mathbf{r}, t) + \nabla \cdot \mathbf{F}(\mathbf{q}) \right] L_j(\mathbf{r}, t) d\Omega = 0 \tag{2.17}$$

Now, let us apply Gauss's theorem over Eq. (2.17) to obtain the local statement:

$$\int_{\Omega_k} \left[ Q \partial_t \mathbf{q}(\mathbf{r}, t) L_j(\mathbf{r}, t) - \mathbf{F}(\mathbf{q}) \cdot \nabla L_j(\mathbf{r}, t) \right] d\Omega = - \int_{\Gamma_{\Omega_k}} \hat{\mathbf{n}} \cdot \mathbf{F}(\mathbf{q}) L_j(\mathbf{r}, t) d\Gamma \tag{2.18}$$

As can be seen in Eq. (2.18), only fields values and derivatives on the element  $\Omega_k$  are involved. It is clear that we have to find a connection between the neighbor elements, because Maxwell's equations are formulated in a continuous space. Consequently, at this point it suffices to substitute the flux  $\mathbf{F}$  by a numerical flux  $\mathbf{F}^*$  as the

unique value to be used at the interface and obtained by combining information from both elements. With this we recover the scheme:

$$\int_{\Omega_k} \left[ Q \partial_t \mathbf{q}(\mathbf{r}, t) L_j(\mathbf{r}, t) - \mathbf{F}(\mathbf{q}) \cdot \nabla L_j(\mathbf{r}, t) \right] d\Omega = - \int_{\Gamma_{\Omega_k}} \hat{\mathbf{n}} \cdot \mathbf{F}^*(\mathbf{q}) L_j(\mathbf{r}, t) d\Gamma \quad (2.19)$$

and applying Gauss' theorem once again, we get:

$$\int_{\Omega_k} \left[ Q \partial_t \mathbf{q}(\mathbf{r}, t) + \nabla \cdot \mathbf{F}(\mathbf{q}) \right] L_j(\mathbf{r}, t) d\Omega = \int_{\Gamma_{\Omega_k}} \hat{\mathbf{n}} \cdot \left[ \mathbf{F}(\mathbf{q}) - \mathbf{F}^*(\mathbf{q}^-, \mathbf{q}^+) \right] L_j(\mathbf{r}, t) d\Gamma \quad (2.20)$$

This is the strong variational formulation of Maxwell's curl equations. In the right hand side of Eq. (2.20),  $\hat{\mathbf{n}}$  represents the outwardly directed normal vector and  $\mathbf{F}^*$  is the numerical flux, which is function of the local element  $\mathbf{q}^-$  and its neighbor  $\mathbf{q}^+$ .

### 2.3.1 Numerical flux

The DG method relies on enforcing continuity of the numerical flux across elements edges, in other words the information through the interface between two elements is carried along the unit normal vector  $\hat{\mathbf{n}}$  [Shu, 2009]. Fig. 2.1 shows the interaction of the flux between two neighbor elements.

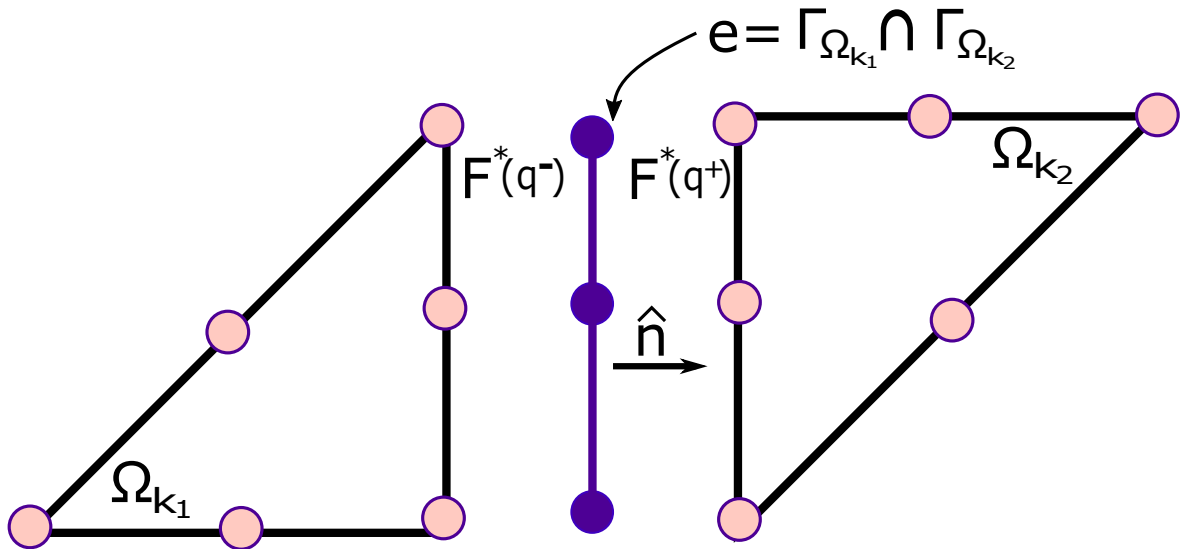


Figure 2.1: Neighbor elements with the same edge  $e$ .

where  $e$  is the interface between elements  $\Omega_{k_1}$  and  $\Omega_{k_2}$ .

An interesting characteristic of DG methods is that we have a lot of possibilities for choosing the numerical flux, for example, centered, upwind and penalized. In the table 2.1 found in [Angulo, 2014], the parameters of each flux mentioned above are:

Table 2.1: Parameters of centered, upwind and penalized numerical fluxes.

| Numerical flux | Centered      | Upwind                  | Penalized                |
|----------------|---------------|-------------------------|--------------------------|
| $A_E$          | $\frac{1}{2}$ | $\frac{Y^+}{Y^- + Y^+}$ | $\frac{Y^+}{Y^- + Y^+}$  |
| $A_H$          | $\frac{1}{2}$ | $\frac{Z^+}{Z^- + Z^+}$ | $\frac{Z^+}{Z^- + Z^+}$  |
| $B_H$          | 0             | $\frac{1}{Y^- + Y^+}$   | $\frac{\tau}{Y^- + Y^+}$ |
| $B_E$          | 0             | $\frac{1}{Z^- + Z^+}$   | $\frac{\tau}{Z^- + Z^+}$ |

Table 2.1 shows the expressions for the  $A$  and  $B$  factors for centered, upwind and penalized numerical fluxes. Terms multiplied by  $B$  are called penalization or upwind terms and come from the solution of the Riemman problem [LeVeque et al., 2002]. On the other hand, for the penalized flux, the factor  $\tau$  is used to avoid the propagation of spurious modes in the computational domain [Hesthaven and Warburton, 2004b]. However, these terms introduce some dissipation to the scheme [Sármány et al., 2007]. One option to mitigate spurious modes is the centered flux, it appears when  $B = 0$  but, at the cost of introducing spectral pollution to the method [Ainsworth et al., 2006]. As a result, the general equation to the numerical Lax-Friedrichs flux is given by:

$$\mathbf{F}^*(\mathbf{q}^-, \mathbf{q}^+) = \begin{cases} \hat{\mathbf{n}} \times \left[ E^- + A_E \Delta E + B_H (\hat{\mathbf{n}} \times \Delta H) \right] \\ \hat{\mathbf{n}} \times \left[ H^- + A_H \Delta H - B_E (\hat{\mathbf{n}} \times \Delta E) \right] \end{cases} \quad (2.21)$$

where  $\Delta E = E^+ - E^-$  and  $\Delta H = H^+ - H^-$ .

Hesthaven and Warburton presented a numerically stable and convergent scheme using the upwind flux [Hesthaven and Warburton, 2002]. It is given by:

$$\hat{\mathbf{n}} \cdot \left[ \mathbf{F}(\mathbf{q}) - \mathbf{F}^*(\mathbf{q}^-, \mathbf{q}^+) \right] = \begin{cases} \bar{Z}^{-1} \left( \alpha \left[ \Delta \mathbf{E} - \hat{\mathbf{n}}(\hat{\mathbf{n}} \cdot \Delta \mathbf{E}) \right] + Z^+ \hat{\mathbf{n}} \times \Delta \mathbf{H} \right) \\ \bar{Y}^{-1} \left( \alpha \left[ \Delta \mathbf{H} - \hat{\mathbf{n}}(\hat{\mathbf{n}} \cdot \Delta \mathbf{H}) \right] - Y^+ \hat{\mathbf{n}} \times \Delta \mathbf{E} \right) \end{cases} \quad (2.22)$$

where  $Z^\pm$  and  $Y^\pm$  are respectively, the impedance and the conductance of the media:

$$Z^\pm = \sqrt{\frac{\mu^\pm}{\varepsilon^\pm}}, \quad Y^\pm = \frac{1}{Z^\pm} = \sqrt{\frac{\varepsilon^\pm}{\mu^\pm}}$$

$\bar{Z}$  and  $\bar{Y}$  are their sums:

$$\bar{Z} = Z^+ + Z^- \quad , \quad \bar{Y} = Y^+ + Y^-$$

In Eqs. (2.21),(2.22) the superscript ” + ” refers to field values from the neighbor element while superscript ” – ” refers to field values from local element. The tangential field components are represented by the normal component of the flux. Hence, the objective of the right hand side in Eq. (2.22) is to enforce the continuity of the tangential field components across the face of the elements.

Another important parameter not yet explained is the upwind term  $\alpha$  in Eq. (2.22). When  $\alpha = 1$  represents the pure upwind flux while for  $\alpha = 0$  we obtain the centered flux. Also, for any number between  $[0, 1]$  we get the penalized flux. Thus, the accuracy of the scheme is influenced by the optimal choice of  $\alpha$ . In [Hesthaven and Warburton, 2007], the authors showed that good convergence rates are achieved using  $\alpha = 1$ , on the contrary, convergence rates are worse for other values of  $\alpha$ . According to Eq. (2.22) the TM mode is given by:

$$\hat{\mathbf{n}} \cdot [\mathbf{F}(\mathbf{q}) - \mathbf{F}^*(\mathbf{q}^-, \mathbf{q}^+)] = \begin{cases} \bar{Z}^{-1} \left( \alpha \Delta \mathbf{E}_z + Z^+ [\mathbf{n}_x \Delta \mathbf{H}_y - \mathbf{n}_y \Delta \mathbf{H}_x] \right) \\ \bar{Y}^{-1} \left( \alpha [\Delta \mathbf{H}_x - \mathbf{n}_x (\mathbf{n}_x \Delta \mathbf{H}_x + \mathbf{n}_y \Delta \mathbf{H}_y)] - Y^+ \mathbf{n}_y \Delta \mathbf{E}_z \right) \\ \bar{Y}^{-1} \left( \alpha [\Delta \mathbf{H}_z - \mathbf{n}_y (\mathbf{n}_x \Delta \mathbf{H}_x + \mathbf{n}_y \Delta \mathbf{H}_y)] + Y^+ \mathbf{n}_x \Delta \mathbf{E}_z \right) \end{cases} \quad (2.23)$$

## 2.3.2 Boundary conditions

Electromagnetic fields are propagating in the whole space continually. However, computational methods cannot discretize an infinite space with a finite quantity of memory. Therefore, computational domain must be truncated. Previously, it was explained that numerical flux can be used to connect adjacent elements, but also serves to directly implement basic boundary conditions in the weak form, only modifying the jumps in factors  $\Delta E$  and  $\Delta H$ .

### 2.3.2.1 Perfect Electric Conductor (PEC)

The PEC condition requires that the tangential component of the electric field must be null and the tangential magnetic field component to be continuous as long as there is not a electric current around the surface.

$$\hat{\mathbf{n}} \times \mathbf{E} = 0 \quad (2.24)$$

In our case to implement the PEC boundary condition, we use the same mirror principle used in [Hesthaven and Warburton, 2002]. To the electric field we assigned

$\mathbf{E}^+ = -\mathbf{E}^-$ . Thus, on a PEC boundary  $\Delta\mathbf{E} = -2\mathbf{E}^-$ . On the other hand, we assigned  $\mathbf{H}^+ = \mathbf{H}^-$  to the magnetic field and consequently,  $\Delta\mathbf{H} = 0$ .

### 2.3.2.2 Perfect Magnetic Conductor (PMC)

The PMC condition is the reciprocal of the PEC one, accordingly:

$$\hat{\mathbf{n}} \times \mathbf{H} = 0 \quad (2.25)$$

As in the PEC boundary conditions, for the PMC we use  $\mathbf{H}^+ = -\mathbf{H}^-$  and  $\mathbf{E}^+ = \mathbf{E}^-$ . Finally, to the PMC case:  $\Delta\mathbf{H} = -2\mathbf{H}^-$  and  $\Delta\mathbf{E} = 0$ .

### 2.3.2.3 Silver-Muller Absorbing (SMA)

The first order SMA boundary condition provides an ideally null reflection coefficient for normal incidence because it is based on assuming that fields outside the computational domain propagate as normal plane waves to the interface [Rao, 1999].

$$\sqrt{\frac{\varepsilon_0}{\mu_0}} \hat{\mathbf{n}} \times \mathbf{E} + \hat{\mathbf{n}} \times (\hat{\mathbf{n}} \times \mathbf{H}) = 0 \quad (2.26)$$

To implement this condition we just have to guarantee that tangential components of the electric and magnetic field to be nulls. It means that  $\Delta\mathbf{E} = -2\mathbf{E}^-$  and  $\Delta\mathbf{H} = -2\mathbf{H}^-$ .

### 2.3.2.4 Sources

When modeling a physical system, it is important to know the geometrical structures or materials of the media. However, the form as the system is illuminated decides if the results has an interesting physic mean or not. For our case, we can incorporate sources directly in the DGTD method via the numerical flux, in the same way as the boundary conditions PEC, PMC and SMA. For this, we have to guarantee that in the position where the input is placed:

$$\mathbf{E}^+ = \mathbf{E}(t), \quad \mathbf{H}^+ = \mathbf{H}(t)$$

where  $\mathbf{E}(t)$  and  $\mathbf{H}(t)$  are the input fields in the time domain.

Then, the flux term can be separated in two: the first term includes the connection among the elements and boundary conditions, and the second one incorporates the source term.

$$\mathbf{F}^{totalflux} = \mathbf{F}^{flux} + \mathbf{F}^{source}$$

## 2.4 Semi-discretized form

We suppose that the local solution can be represented in the following form:

$$\mathbf{q}_k^h = \sum_{i=1}^{N_p} q_i(\mathbf{r}_i, t) L_i(\mathbf{r}) = \sum_{n=1}^{N_p} \hat{q}_n \psi_n(\mathbf{r}) \quad (2.27)$$

where  $L_i$  and  $\psi_n$  determine a nodal and modal local basis, respectively.

According to [Hesthaven and Warburton, 2007], the nodal and modal coefficients can be related as follows:

$$q_{nodal} = V \hat{q}_{modal} \quad (2.28)$$

This matrix,  $V$ , is known as a generalized Vandermonde matrix,  $V_{ij} = \psi_j(\mathbf{r}_i)$ . Its function is to establish the connection between the modes  $\hat{q}$  and the nodal values  $q$ . Now, we choose the interpolating Lagrange polynomial to the function  $L_i$  because it is well known that this polynomial basis has the Kronecker delta property:

$$L_i(\mathbf{r}_j) = \begin{cases} 1, & i = j \\ 0, & i \neq j \end{cases} \quad (2.29)$$

Lagrange polynomials are formed by the linear combination of monomials and can be represented in general by [Busch et al., 2011]:

$$L_i(\mathbf{r}_j) = \sum_{k,l,m=0}^{k+l+m \leq N} a_{k,l,m}^i x^k y^l z^m \quad (2.30)$$

where  $N$  is the polynomial order. The grid point nodes  $N_p$  in each element have to respect the condition:

$$N_p = N + 1 \quad (1D)$$

$$N_p = \frac{1}{2}(N + 1)(N + 2) \quad (2D)$$

$$N_p = \frac{1}{6}(N + 1)(N + 2)(N + 3) \quad (3D)$$

To guarantee numerical stable behavior of the generalized Vandermonde matrix  $V$ , an orthonormal polynomial basis for  $\psi_j(\mathbf{r})$  must be used. In this work we used the same basis as in [Hesthaven and Warburton, 2002]. So, let us consider a canonical basis

defined on a space with the coordinates  $(r, s)$ :

$$\begin{aligned} \psi_m(\mathbf{r}) &= r^i s^j, \quad (i, j) \geq 0; \quad i + j \leq N \\ m &= j + (N + 1)i + 1 - \frac{i}{2}(i - 1), \quad (i, j) \geq 0; \quad i + j \leq N \end{aligned} \quad (2.31)$$

It cannot be expected that the Eq. (2.31) is a good choice because if the polynomial order  $N$  increases, the vandermonde matrix becomes poorly conditioned. To solve this problem, the polynomial basis can be orthonormalized applying the Gram-Schmidt process. The resulting basis is:

$$\psi_m(\mathbf{r}) = \sqrt{2} P_i^\alpha(a) P_j^{\beta(2i+1,0)}(b) (1-b)^i \quad (2.32)$$

where

$$a = 2 \frac{1+r}{1-s} - 1, \quad b = s,$$

and  $P_n^{\alpha,\beta}$  is the  $n$ -th order Jacobi polynomial. When  $\alpha = \beta = 0$  it is the Legendre polynomial.

### 2.4.1 Nodal distribution

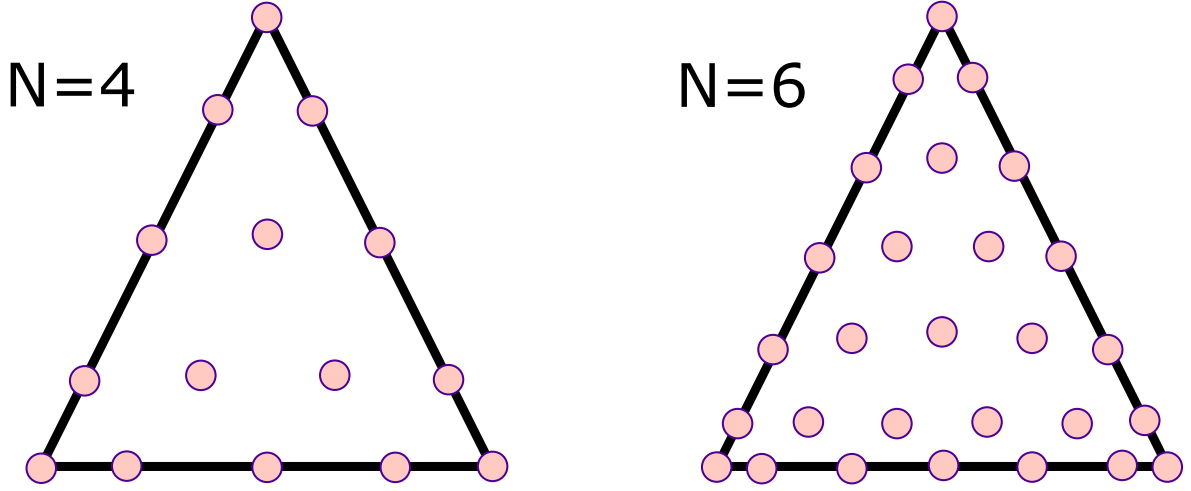
We have to choose an optimal distribution of the  $N_p$  grid point nodes. This choice is very important because a poorly chosen set generates computational problems as ill-conditioning matrices.

As in FEM, the nodal distribution is done in a reference element and then, nodes are mapped into a physical element. There are some different ways to build a good nodal distribution [Hesthaven, 1998; Taylor et al., 2000; Chen and Babuška, 1995]. However, all of them require substantial initial effort and it is a disadvantage that we want to avoid. In [Hesthaven and Warburton, 2007], a simple and constructive approach was built for a computation of a well-behaved family of nodal points of any order. This process maps a set of equidistant nodes into Legendre-Gauss-Lobatto distribution. Finally, the nodal distribution is calculated for each simulation, using a computational low cost algorithm and avoiding distribution tables. Fig. 2.2 shows the  $N_p$  grid point nodes into a triangle for two different polynomial orders.

### 2.4.2 Mass and stiffness matrices

Now, to the spatial discretization of the TM mode, we take the left hand side of Eq. (2.10), remembering that flux term can be written as Eq. (2.15). Considering only a



Figure 2.2: Nodal distribution for  $N = 4$  and  $6$ .

local element  $k$ :

$$\int_{\Omega_k} \left[ Q^k \partial_t \mathbf{q}^k + \nabla \cdot \mathbf{F}(\mathbf{q}^k) \right] L_j^k d\Omega = \int_{\Omega_k} \left[ Q^k \partial_t \mathbf{q}^k + A_x \partial_x \mathbf{q}^k + A_y \partial_y \mathbf{q}^k \right] L_j^k d\Omega \quad (2.33)$$

The approximation of each variable in the system is made using basis functions such that:  $u_h^k = \sum_{i=1}^{N_p} u_t^{k,i} L_i^k(x, y)$ , where  $N_p$  are number of the unknown variables for each element. Coefficients depend on time and the basis functions of space. Therefore, using expansion by basis functions in Eqs. (2.15), we obtain:

$$\begin{aligned} \int_{\Omega_k} \left( \varepsilon^k \partial_t E_z^k - \partial_x H_y^k + \partial_y H_x^k \right) L_j^k d\Omega &= \varepsilon^k \mathcal{M}^k \partial_t \mathbf{E}_z^k - [\mathcal{S}^{k,x}]^T \mathbf{H}_y^k + [\mathcal{S}^{k,y}]^T \mathbf{H}_x^k \\ \int_{\Omega_k} \left( \mu_0^k \partial_t H_x^k + \partial_y E_z^k \right) L_j^k d\Omega &= \mu_0^k \mathcal{M}^k \partial_t \mathbf{H}_x^k + [\mathcal{S}^{k,y}]^T \mathbf{E}_z^k \\ \int_{\Omega_k} \left( \mu_0^k \partial_t H_y^k - \partial_x E_z^k \right) L_j^k d\Omega &= \mu_0^k \mathcal{M}^k \partial_t \mathbf{H}_y^k - [\mathcal{S}^{k,x}]^T \mathbf{E}_z^k \end{aligned} \quad (2.34)$$

where  $\mathbf{E}_z^k, \mathbf{H}_x^k, \mathbf{H}_y^k$  are vectors with dimension  $N_p \times 1$ , they contain the field component for each nodal value. Moreover, electric permittivity  $\varepsilon^k$  and magnetic permeability  $\mu_0^k$  have the same dimension  $N_p \times 1$  with the information about the media in element  $k$ . On the other hand,  $\mathcal{M}^k$  and  $\mathcal{S}^k$  are known as mass and stiffness matrices respectively. Their dimensions are equal to  $N_p \times N_p$ .

$$\begin{aligned} \mathcal{M}_{i,j}^k &= \int_{\Omega_k} L_i^k L_j^k d\Omega \\ \mathcal{S}_{i,j}^{k,x} &= \int_{\Omega_k} \partial_x L_i^k L_j^k d\Omega \\ \mathcal{S}_{i,j}^{k,y} &= \int_{\Omega_k} \partial_y L_i^k L_j^k d\Omega \end{aligned} \quad (2.35)$$

Taking into account that  $V$  was built using an orthonormal basis, mass matrix can be calculated as follows:

$$\mathcal{M}^k = J^k(VV^T)^{-1} \quad (2.36)$$

Where  $J^k$  is the jacobian of the element  $k$ . It is important to say that the mass matrix is diagonal due to the use of orthonormal polynomials  $\psi_m$ . Now, to calculate the stiffness matrix, we need the differentiation matrices:

$$\frac{\partial}{\partial x} = \frac{\partial r}{\partial x} \mathcal{D}_r + \frac{\partial s}{\partial x} \mathcal{D}_s, \quad \frac{\partial}{\partial y} = \frac{\partial r}{\partial y} \mathcal{D}_r + \frac{\partial s}{\partial y} \mathcal{D}_s$$

where  $\mathcal{D}_r$  and  $\mathcal{D}_s$  calculate derivatives in the reference space  $(r, s)$ . They can be calculated as follows:

$$V_{r,(i,j)} = \frac{\partial \psi_j(r_i, s_i)}{\partial r}$$

$$V_{s,(i,j)} = \frac{\partial \psi_j(r_i, s_i)}{\partial s}$$

Then, we have the relation  $\mathcal{D}_r = V_r V^{-1}$  and  $\mathcal{D}_s = V_s V^{-1}$ . Finally, the expressions for the stiffness matrices are:

$$\mathcal{S}^{k,x} = \left( \frac{\partial r}{\partial x} \mathcal{D}_r + \frac{\partial s}{\partial x} \mathcal{D}_s \right) (VV^T)^{-1}$$

$$\mathcal{S}^{k,y} = \left( \frac{\partial r}{\partial y} \mathcal{D}_r + \frac{\partial s}{\partial y} \mathcal{D}_s \right) (VV^T)^{-1} \quad (2.37)$$

### 2.4.3 Flux discretization

Until now, the computation of the local matrices for the left hand side of Eq. (2.15) has been explained. Also, we have to explain how to discretize the flux term of Eq. (2.20) to complete semi-discretized form. So, firstly we consider that:

$$\hat{\mathbf{n}} \cdot \mathbf{F}(\mathbf{q}) - \mathbf{F}^*(\mathbf{q}^-, \mathbf{q}^+) = F \Delta \mathbf{q} \quad (2.38)$$

Substituing Eq. (2.38) in the righth hand side of Eq. (2.20):

$$\int_{\Gamma_{\Omega_k}} \hat{\mathbf{n}} \cdot \left[ \mathbf{F}(\mathbf{q}^k) - \mathbf{F}^*(\mathbf{q}^-, \mathbf{q}^+) \right] L_j^k d\Gamma = \int_{\Gamma_{\Omega_k}} F \Delta \mathbf{q} L_j^k d\Gamma \quad (2.39)$$

Taking into consideration that all edges in a triangular element are boundary, it can be said that each edge is an intersection between local and neighbor element. So:

$$\int_{\Gamma_{\Omega_k}} F \Delta \mathbf{q} L_j^k d\Gamma = \sum_{e=1}^3 \int_{edge} F_e (\mathbf{q}^{+e} - \mathbf{q}^{-e}) L_j^k d\Gamma \quad (2.40)$$

Now, we have to discretize as before  $\mathbf{q}^{+e}$  and  $\mathbf{q}^{-e}$ , therefore:

$$\sum_{e=1}^3 \int_{edge} F_e(\mathbf{q}^{+e} - \mathbf{q}^{-e}) L_j^k d\Gamma = \sum_{e=1}^3 F_e \mathcal{M}_{1d}^e(\mathbf{q}_t^{+e} - \mathbf{q}_t^{-e}) \quad (2.41)$$

where  $\mathcal{M}_{1d}^e$  is a diagonal block matrix with dimension  $3N \times 3N$  and each block is the called edge-mass matrix  $\mathcal{M}^e$  whose form is:

$$\mathcal{M}_{i,j}^e = \int_{edge} L_i^k L_j^k d\Gamma \quad (2.42)$$

Furthermore, there is another way to calculate  $\mathcal{M}^e$  because the functions  $\psi_m$  in edges are also orthonormal polynomials. According to [Hesthaven and Warburton, 2007], functions  $\psi_m^e$  over an edge  $e$  are given by:

$$\psi_m^e(\mathbf{r}) = \frac{P_{m-1}(\mathbf{r})}{\sqrt{\gamma_m - 1}} \quad (2.43)$$

where  $P_m$  are the classic Legendre polynomials of order  $m$  and  $\gamma_m$  is a normalization factor.

$$\gamma_m = \frac{2}{2m + 1} \quad (2.44)$$

Now, considering that the Vandermonde one-dimensional matrix is equal to  $V_{1d,(i,j)} = \psi_j(\mathbf{r}_i)$ , the edge-mass matrix can be calculated by:

$$\mathcal{M}^e = \frac{h^e}{2} (V_{1d} V_{1d}^T)^{-1} \quad (2.45)$$

where  $h^e$  is the length of the triangle edge.

## 2.5 Low-Storage Explicit Runge Kutta fourth order method for time integration

Until now the space discretization using the discontinuous Galerkin approach has been presented. However, our model depends on the space as well as on time. In this case, for the time integration, we use the low-storage five-stage fourth-order explicit Runge-Kutta method (LSERK4) [Williamson, 1980; Hesthaven and Warburton, 2004a; Diehl et al., 2010]. This method is one of the most used in high order DG schemes because it does not need to compute and evaluate derivatives and also, produces low dispersion and dissipation errors [Angulo, 2014]. As in all time-stepping methods, the aim is to

find the solution in the time step  $t_{n+1}$  taking as a reference the solution at the first time step  $t_n$ , starting with the given initial condition. Then, considering the approximate solution  $\mathbf{q}_h$ :

$$\frac{d\mathbf{q}_h}{dt} = \mathcal{L}(\mathbf{q}_h, t)$$

and applying the LSERK4 method we have:

$$i \in [1, \dots, 5] : \begin{cases} \mathbf{p}^{(0)} = \mathbf{q}_h^n \\ \beta^{(i)} = a_i \beta^{(i-1)} + \Delta t \mathcal{L}(\mathbf{p}^{(i-1)}, t_n + c_i \Delta t) \\ \mathbf{p}^{(i)} = \mathbf{p}^{(i-1)} + b_i \beta^{(i)} \\ \mathbf{q}_h^{n+1} = \mathbf{p}^{(5)} \end{cases} \quad (2.46)$$

where  $\mathbf{q}_h^n$  and  $\mathbf{q}_h^{n+1}$  are respectively, initial and final solution. They are separated by the time step  $\Delta t$ . Coefficients  $a_i$ ,  $b_i$  and  $c_i$  can be found in [Hesthaven and Warburton, 2007].

### 2.5.1 Conditional stability and time step

The LSERK4, as his name says, is a explicit method and therefore is subject to conditional stability, also known as the Courant-Friedrichs-Lewy condition (CFL condition). When the time step  $\Delta t$  exceeds a critical value, the solution is subject to unphysical exponential growth. The size of the time step is directly related with the quality of the mesh, as the very popular FDTD method [Busch et al., 2011]. One interesting approach was found in [Hesthaven and Warburton, 2007], where the time step is calculated with the minimum distance between the nodes in element  $k$ :

$$\Delta t \leq \frac{C}{c_k} \min_{k,i} \frac{\Delta h_{ki}}{2} \quad (2.47)$$

where  $\min_{k,i} \Delta h_{ki}$  indicates the minimum distance among nodes in  $k$ ,  $c_k$  is the maximum speed of light in  $k$  and  $C$  is the CFL constant.

# Chapter 3

## Curved Elements

In the previous Chapter the whole scheme for the DGTD method was explained, including the steps for spatial and temporal discretization. This formulation is valid only using the well-known straight side triangles, these elements can represent accurately any surface but their size can be very small to capture small features. Similar to the finite element method (FEM) [Monk et al., 2003], DGTD uses unstructured meshes that adapt to any geometry. However, curved surfaces need a big quantity of small size elements to approximate them. As a consequence, the maximum stable time step is affected drastically. For this reason, it makes sense to introduce the CE [Fahs, 2010; Hille et al., 2010] with the objective of avoiding very small elements, reducing the number of them and at the same time increasing the accuracy of the geometrical representation.

### 3.1 Strong variational form for the CE

According to [Zhang, 2016], we consider the same domain  $\Omega$  rounded by the boundary  $\Gamma$  as in Section 2.3. For simplicity, we assume that  $\Gamma$  does not intersect more than two vertices of any triangle in  $\Omega$ . Hence, for any boundary triangle  $K$  adjacent to the curve boundary  $\Gamma$ , there are two cases of CEs depending on the intersection between the curve  $\Gamma$  and boundary triangle  $K$ . If  $\Gamma$  intersects  $K$  at its interior, it is called a concave case. Otherway, it is known as convex case. Let us call  $e^i$  ( $i = 1, 2, 3$ ) as the three edges of triangle  $K$  and assuming that  $e^1$  is the one adjacent to  $\Gamma$ . Then, we assume that  $\tilde{e}^1$  is an approximated representation of  $\Gamma$ . We use  $\tilde{K}$  to denote the CE bounded by  $e^2$ ,  $e^3$  and  $\tilde{e}^1$ . Finally,  $C$  is the difference between  $K$  and  $\tilde{K}$ . These geometrical aspects can be seen in Fig . 3.1.

The variational formulation showed in section 2.3 is valid for all straight side elements, nevertheless, we have to do some modifications for the curved elements. So,

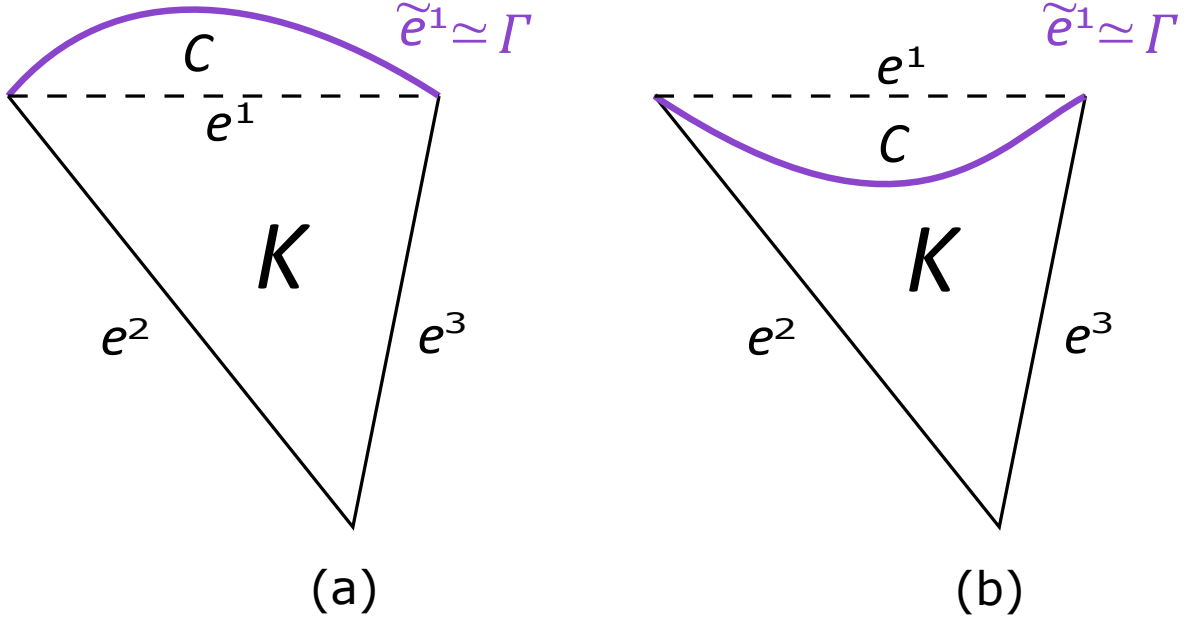


Figure 3.1: Two possible cases of boundary triangle  $K$ . (a) Convex case, (b) Concave case.

considering Eq. (2.10) and remembering that we assumed  $S = 0$ , the equation can be rewritten as:

$$Q \frac{\partial \mathbf{q}}{\partial t} = -\nabla \cdot \mathbf{F}(\mathbf{q}) \quad (3.1)$$

Also, rewriting Eq. (2.20), we obtain the equivalent strong formulation for a CE:

$$\int_{\tilde{K}} \left[ Q \partial_t \mathbf{q} + \nabla \cdot \mathbf{F}(\mathbf{q}) \right] L_j d\Omega + \int_{\partial \tilde{K}} \hat{\mathbf{n}} \cdot \left[ \mathbf{F}^*(\mathbf{q}^-, \mathbf{q}^+) - \mathbf{F}(\mathbf{q}) \right] L_j d\Gamma = 0 \quad (3.2)$$

where for this case  $\hat{\mathbf{n}}$  is the outward unit normal vector to the boundary  $\partial \tilde{K}$ .

Moreover, we have two expressions for the flux term, first one appears when adjacent triangles share straight edges  $K_i (i = 2, 3)$ , another one appears when edge shared is the curved one  $K_1$ . See Fig. 3.2.

So, the numerical Lax-Friedrichs flux after some modifications is given by:

$$\mathbf{F}^*(\mathbf{q}^-, \mathbf{q}^+)_{e^i} = \begin{cases} \hat{\mathbf{n}}_{e^i} \times \left[ E^- + A_E \Delta E + B_H \left( \hat{\mathbf{n}}_{e^i} \times \Delta H \right) \right] \\ \hat{\mathbf{n}}_{e^i} \times \left[ H^- + A_H \Delta H - B_E \left( \hat{\mathbf{n}}_{e^i} \times \Delta E \right) \right] \end{cases}, \quad i = 2, 3 \quad (3.3)$$

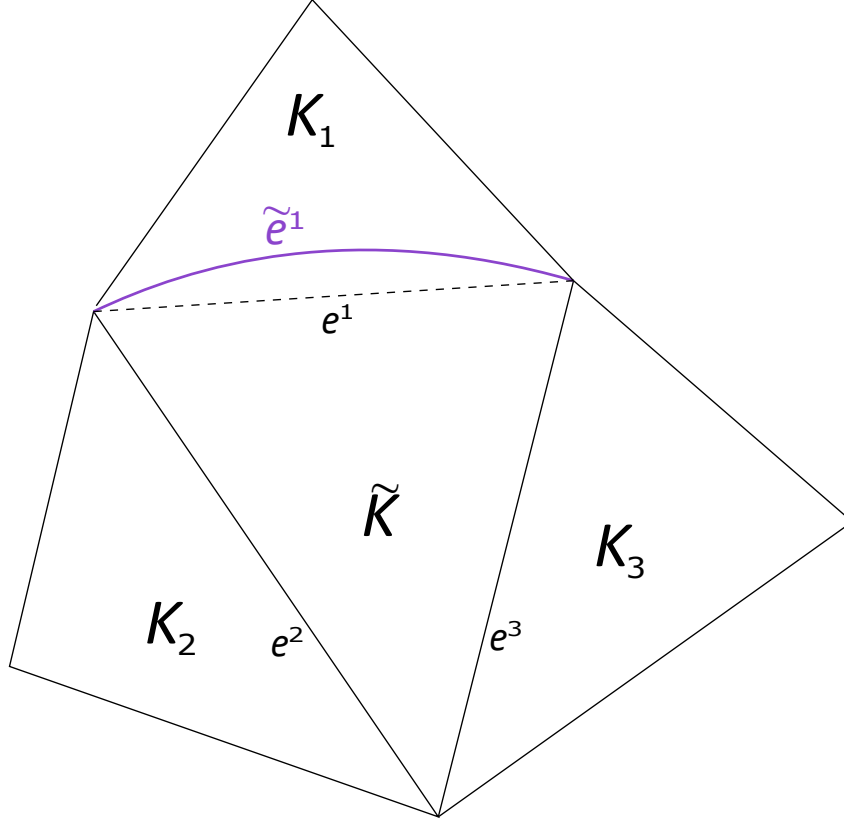


Figure 3.2: CE with neighbor elements

and

$$\mathbf{F}^*(\mathbf{q}^-, \mathbf{q}^+)_{\tilde{e}^1} = \begin{cases} \hat{\mathbf{n}}_{\tilde{e}^1} \times \left[ E^- + A_E \Delta E + B_H \left( \hat{\mathbf{n}}_{\tilde{e}^1} \times \Delta H \right) \right] \\ \hat{\mathbf{n}}_{\tilde{e}^1} \times \left[ H^- + A_H \Delta H - B_E \left( \hat{\mathbf{n}}_{\tilde{e}^1} \times \Delta E \right) \right] \end{cases} \quad (3.4)$$

### 3.1.1 Convex case

As can be seen in Fig. 3.1, the convex case happens when  $\Gamma$  intercepts  $K$  at outside of it and, therefore,  $\tilde{K} = K \cup C$ . Taking into consideration Eq. (2.19), for the convex case we have:

$$\int_K \left[ Q \partial_t \mathbf{q} L_j - \mathbf{F}(\mathbf{q}) \cdot \nabla L_j \right] d\Omega + \int_{\partial \tilde{K}} \hat{\mathbf{n}} \cdot \mathbf{F}^*(\mathbf{q}) L_j d\Gamma = \int_C \left[ -Q \partial_t \mathbf{q} L_j + \mathbf{F}(\mathbf{q}) \cdot \nabla L_j \right] d\Omega \quad (3.5)$$

Inserting Eq. (3.1) in the right hand-side of Eq. (3.5):

$$\int_C \left[ -Q \partial_t \mathbf{q} L_j + \mathbf{F}(\mathbf{q}) \cdot \nabla L_j \right] d\Omega = \int_C \left[ \nabla \cdot \mathbf{F}(\mathbf{q}) L_j + \mathbf{F}(\mathbf{q}) \cdot \nabla L_j \right] d\Omega$$

and applying Gauss's theorem, the right hand side of Eq. (3.5) becomes:

$$\int_C \left[ \nabla \cdot \mathbf{F}(\mathbf{q})L_j + \mathbf{F}(\mathbf{q}) \cdot \nabla L_j \right] d\Omega = \int_{\partial C} \mathbf{F}(\mathbf{q}) \cdot \hat{\mathbf{n}}(C)L_j d\Gamma \quad (3.6)$$

where  $\hat{\mathbf{n}}(C)$  denotes the outward unit normal vector to the boundary  $\partial C$ . Now, replacing Eq. (3.6) in the right hand side of Eq. (3.5), we get the weak formulation in the convex case for a boundary triangle  $K$ .

$$\int_K \left[ Q\partial_t \mathbf{q}L_j - \mathbf{F}(\mathbf{q}) \cdot \nabla L_j \right] d\Omega + \int_{\partial \tilde{K}} \hat{\mathbf{n}} \cdot \mathbf{F}^*(\mathbf{q})L_j d\Gamma = \int_{\partial C} \mathbf{F}(\mathbf{q}) \cdot \hat{\mathbf{n}}(C)L_j d\Gamma \quad (3.7)$$

Finally, we apply integration by parts in Eq. (3.7) and using the relation  $\hat{\mathbf{n}}(C) = \hat{\mathbf{n}}$ . After the cancellation of the line integral along the edge  $e^1$ , the strong formulation in the convex case can be written as:

$$\int_K \left[ Q\partial_t \mathbf{q} + \nabla \cdot \mathbf{F}(\mathbf{q}) \right] L_j d\Omega + \int_{\partial \tilde{K}} \hat{\mathbf{n}} \cdot \left[ \mathbf{F}^*(\mathbf{q}^-, \mathbf{q}^+) - \mathbf{F}(\mathbf{q}) \right] L_j d\Gamma = 0 \quad (3.8)$$

### 3.1.2 Concave case

As can be seen in Fig. 3.1, the concave case happens when  $\Gamma$  intercepts  $K$  at inside of it. Therefore,  $K = \tilde{K} \cup C$ . Taking into consideration Eq. (2.19), for the concave case we have:

$$\int_K \left[ Q\partial_t \mathbf{q}L_j - \mathbf{F}(\mathbf{q}) \cdot \nabla L_j \right] d\Omega + \int_{\partial \tilde{K}} \hat{\mathbf{n}} \cdot \mathbf{F}^*(\mathbf{q})L_j d\Gamma = \int_C \left[ Q\partial_t \mathbf{q}L_j - \mathbf{F}(\mathbf{q}) \cdot \nabla L_j \right] d\Omega \quad (3.9)$$

Now, the same convex case steps are applied, replacing Eq. (3.1) in the right hand side of Eq. (3.9), we obtain:

$$\int_C \left[ Q\partial_t \mathbf{q}L_j - \mathbf{F}(\mathbf{q}) \cdot \nabla L_j \right] d\Omega = - \int_C \left[ \nabla \cdot \mathbf{F}(\mathbf{q})L_j + \mathbf{F}(\mathbf{q}) \cdot \nabla L_j \right] d\Omega$$

and applying Gauss's theorem, the right hand side of Eq. (3.9) becomes:

$$- \int_C \left[ \nabla \cdot \mathbf{F}(\mathbf{q})L_j + \mathbf{F}(\mathbf{q}) \cdot \nabla L_j \right] d\Omega = - \int_{\partial C} \mathbf{F}(\mathbf{q}) \cdot \hat{\mathbf{n}}(C)L_j d\Gamma \quad (3.10)$$

where  $\hat{\mathbf{n}}(C)$  denotes the outward unit normal vector to the boundary  $\partial C$ . Now, re-



placing Eq. (3.10) in the right hand side of Eq. (3.9), we get the weak formulation in the concave case for a boundary triangle  $K$ .

$$\int_K \left[ Q \partial_t \mathbf{q} L_j - \mathbf{F}(\mathbf{q}) \cdot \nabla L_j \right] d\Omega + \int_{\partial \tilde{K}} \hat{\mathbf{n}} \cdot \mathbf{F}^*(\mathbf{q}) L_j d\Gamma = - \int_{\partial C} \mathbf{F}(\mathbf{q}) \cdot \hat{\mathbf{n}}(C) L_j d\Gamma \quad (3.11)$$

Finally, we apply integration by parts in Eq. (3.11) and using the relation  $\hat{\mathbf{n}}(C) = -\hat{\mathbf{n}}$ , the strong formulation in the concave case can be written exactly as Eq. (3.8).

As a consequence of CE, the strong formulation showed in Eq. (2.20) has to be modify. Therefore, the generalized strong formulation for a curved element  $\tilde{K}$  is given by the next equation:

$$\begin{aligned} \int_K \left[ Q \partial_t \mathbf{q} + \nabla \cdot \mathbf{F}(\mathbf{q}) \right] L_j d\Omega + \sum_{i=2}^3 \int_{e^i} \hat{\mathbf{n}} \cdot \left[ \mathbf{F}(\mathbf{q}) - \mathbf{F}^*(\mathbf{q}^-, \mathbf{q}^+) \right] L_j \partial \tilde{K}_{e^i} \\ + \int_{\tilde{e}^1} \hat{\mathbf{n}}(\tilde{K}) \cdot \left[ \mathbf{F}(\mathbf{q}) - \mathbf{F}^*(\mathbf{q}^-, \mathbf{q}^+) \right] L_j \partial \tilde{K}_{\tilde{e}^1} = 0 \end{aligned} \quad (3.12)$$

where  $\hat{\mathbf{n}}$  denotes the outward unit normal vector for straight side edges of the triangle  $\tilde{K}$ . Also,  $\hat{\mathbf{n}}(\tilde{K})$  denotes the outward unit normal vector for curved edge that can be positive or negative, depending on the form of the CE.

## 3.2 Forming curved elements

A lot of mesh generators use unstructured meshes to represent complex geometries, for example [Persson and Strang, 2004; Shewchuk, 1996]. However, we cannot expect that they place automatically the nodes on curved surfaces. Hence, in this Section, we explain the required steps to modify straight side elements located near to a curved boundary.

First, we have to identify all the elements with at least one face near to the curved boundary and both the face number. Second, verify if vertices and faces nodes are located exactly onto the curved boundary. Third, apply the deformation over internal nodes of the curved elements and update the volume node locations.

Fig. 3.3 shows an example of a node deformation process for an element of order six with an edge over the curved boundary. As can be seen in Fig. 3.3, the vertices in the element are located exactly over the unit circle. Moreover, the nodes on the interior of the curved face are redistributed by arc-length along the segment of the

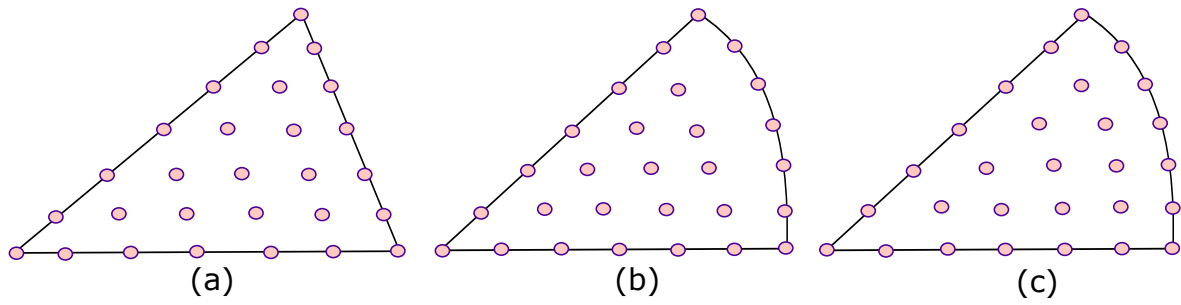


Figure 3.3: (a) Straight side element. (b) Nodes deformed on the face curved. (c) Final nodes distribution in the CE

curved boundary between two vertices. Last, we apply the deformation to redistribute all inner nodes in the element.

Once the vertices nodes of all CE are correctly positioned, we have to adjust the nodes of the finite element mesh. This is important because we have to guarantee that the modification is made on all the elements that share these vertices. The next step is to parameterize each curved segment and find the polar angles of vertices of curved faces, these angles are calculated relative to the polar coordinates of the center of the circle. See Fig. 3.4.

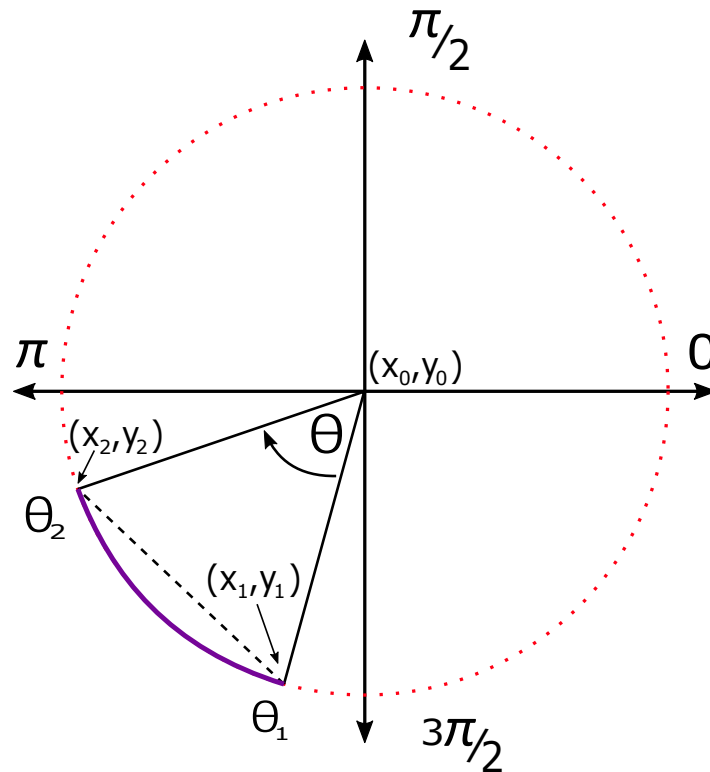


Figure 3.4: Straight side element near to curved boundary

where  $\theta_1$  and  $\theta_2$  are the polar angles of the vertices of curves faces. we calculate them

as follows:

$$\theta_1 = \tan^{-1} \left( \frac{y_1 - y_0}{x_1 - x_0} \right), \quad \theta_2 = \tan^{-1} \left( \frac{y_2 - y_0}{x_2 - x_0} \right)$$

Previously, we said that the Legendre-Gauss-Lobatto distribution is used for the nodal basis. Therefore, we have to maintain the same distribution for the nodes on the curved faces to avoid severe distortion of the volume nodes and, consequently, destroy the nodal basis approximation. Next, we create a distribution of polar angles between  $\theta_1$  and  $\theta_2$ . Also, in some cases, we have to apply an angle shifting based on the location of the element in relation to the center of the circle. Finally, we apply the deformation on the interior nodes of CE using the same concept of [Gordon and Hall, 1973]. Basically, we use the called deformation functions depending on the faces that need to be curved. This deformation is zero on the other two faces of each triangle.

### 3.3 Operators on curved elements

As was explained in Section 2.4, the generalized vandermonde matrix is used to compute inner products needed in the implementation of the DG method. This matrix was constructed with orthonormal polynomial basis functions. However, this approach is not successful when the range of integration does not coincide with the range of the orthonormal polynomials. Therefore, in this Section, we are going to explain how the integrals of nonpolynomial functions are treated.

When working with CE, we must consider integral of nonpolynomial functions because jacobians are non constant in each curved element, therefore, it is recommended to use cubature formulas to evaluate the elemental inner products. A cubature is a multidimensional version of the classic quadrature formula, then, a cubature is a set of  $N_c$  two dimensional points  $\{r_i^c, s_i^c\}_{i=1}^{N_c}$  with  $N_c$  associated weights  $\{w_i^c\}_{i=1}^{N_c}$ , where the number of points  $N_c$  depends on the maximum order of polynomial required to be integrated accurately. There are a lot of cubature formulas, a survey where many different methods are reviewed can be found in [Cools and Rabinowitz, 1993; Cools, 1999; Stroud, 1971]. Nevertheless, in this work are used the symmetric rules proposed in [Wandzurat and Xiao, 2003].

The inner product on a reference triangle can be approximated by two functions  $f$  and  $g$ , using a  $N$ -th-order cubature with  $N_c(N)$  nodes, we have:

$$(f, g)_{D^k} \approx \sum_{i=1}^{N_c} g(r_i^c, s_i^c) f(r_i^c, s_i^c) J_i^k w_i^c \quad (3.13)$$

where  $J_i^k$  is the jacobian of the polynomial map from the reference element to the physical element

$$J_i^k = \left( \frac{\partial x^k}{\partial r} \frac{\partial y^k}{\partial s} - \frac{\partial x^k}{\partial s} \frac{\partial y^k}{\partial r} \right)_{(r_i^c, s_i^c)}$$

Remembering that  $(x, y)$  are polynomial function of  $(r, s)$  for the curved elements. We assumed that the coordinate transform relies on an isoparametric map of the form:

$$x^k(r, s) = \sum_{i=1}^{N_p} \psi_i(r, s) x_i^k, \quad y^k(r, s) = \sum_{i=1}^{N_p} \psi_i(r, s) y_i^k$$

where the polynomial basis  $\{\psi_i\}_{i=1}^{N_p}$  is the known interpolating Lagrange polynomial, discussed in Section 2.4. The coefficients  $(x_i^k, y_i^k)$  are the physical location of each node on the CE. Now, to evaluate geometric factors at the cubature nodes, we need the derivatives of Lagrange interpolants, these can be computed by:

$$\begin{aligned} \frac{\partial x^k}{\partial r} (r_i^c, s_i^c) &= \sum_{j=1}^{N_p} \frac{\partial L_j^k}{\partial r} (r_i^c, s_i^c) x_j^k, & \frac{\partial x^k}{\partial s} (r_i^c, s_i^c) &= \sum_{j=1}^{N_p} \frac{\partial L_j^k}{\partial s} (r_i^c, s_i^c) x_j^k \\ \frac{\partial y^k}{\partial r} (r_i^c, s_i^c) &= \sum_{j=1}^{N_p} \frac{\partial L_j^k}{\partial r} (r_i^c, s_i^c) y_j^k, & \frac{\partial y^k}{\partial s} (r_i^c, s_i^c) &= \sum_{j=1}^{N_p} \frac{\partial L_j^k}{\partial s} (r_i^c, s_i^c) y_j^k \end{aligned} \quad (3.14)$$

Moreover, the computation of the element boundary flux must be changed. For the surface integrals, we created a one dimensional Gauss quadrature [Golub and Welsch, 1969] on each face of each element. Now, to simplify the implementation process, interpolation matrices are created on the reference element and then, interpolated from the node data of the CE to the nodes on the reference element and Gauss nodes on each face. Finally, to evaluate the derivatives matrices, we have:

$$\begin{aligned} \mathcal{D}_{x, D^k} &\approx (V^c)^T \mathcal{W} V^c \mathcal{D}_x \\ \mathcal{D}_{y, D^k} &\approx (V^c)^T \mathcal{W} V^c \mathcal{D}_y \end{aligned} \quad (3.15)$$

where  $V_{ij}^c = L_j(r_i^c, s_i^c)$ ,  $\mathcal{W}$  is a diagonal matrix with entries  $\mathcal{W}_{ii} = w_i^c J_i^c$  and  $\mathcal{D}_x, \mathcal{D}_y$  are the derivatives matrices calculated with the cubature data. Finally, this scheme has to be applied individually for each curved element due to the nonconstant jacobian.

# Chapter 4

## Results and Discussion

In this section, we consider various wave propagation problems in homogeneous and heterogeneous media to evaluate the benefits of applying the CE in the DGTD scheme. In the first problem, we show the solution of a concentric PEC cylinders resonator with the purpose to check the accuracy and to validate the method. These results are shown in terms of convergence rate and global  $L^2$  error. Next, we show the analysis of two very common scattering problems (e.g. scattering by a PEC circular cylinder, scattering by a dielectric circular cylinder). These problems have a convergence analysis similar to the previous one. Then, we forced the method solving a more complicated scattering problem with more than one scatter (e.g. scattering by a PEC coated circular cylinder). Finally, it has been solved a more realistic engineering problem that involves a lot of dielectric circular cylinders, showing that DGTD with curved element is a powerful numerical technique. To evaluate the accuracy of the numerical scheme, we compute the difference between the exact solution, let say  $E$ , and the approximate solution  $E_h$  using the  $L^2$  norm, see Eq. (4.1). On the other hand, for the convergence analysis, we use the Eq. (4.2), where  $h_i$  and  $h_{i+1}$  are two different values of the size of the mesh and  $\delta(h_i)$ ,  $\delta(h_{i+1})$  are the errors corresponding to a mesh of size  $h_i$  and  $h_{i+1}$ , respectively.

$$e_r = \int_{\Omega} \sqrt{\frac{(E - E_h)^2}{E}} d\Omega \quad (4.1)$$

$$\beta = \frac{\log\left[\frac{\delta(h_{i+1})}{\delta(h_i)}\right]}{\log\left[\frac{h_i}{h_{i+1}}\right]} \quad (4.2)$$

## 4.1 Concentric PEC cylinders resonator

As can be seen in Fig. 4.1, we consider a resonator that consists of two concentric PEC cylinders with an electromagnetic wave that bounces back and forth between the walls. The material inside the cylinders is considered vacuum  $\varepsilon_r = \mu_r = 1$ . The radius of the cylinders are  $r_1 = 1/6$  m and  $r_2 = 1/2$  m. According to [Ditkowski et al., 2001], the exact time domain solution to this problem is given by:

$$E_z = \cos(\omega t + \theta) [J_1(\omega r) + aY_1(\omega r)]$$

$$H_x = -\frac{1}{2}\sin(\omega t + \theta)\sin(\theta) [J_0(\omega r) - J_2(\omega r) + a(Y_0(\omega r) + Y_2(\omega r))] \\ -\frac{\cos(\theta)}{\omega r}\cos(\omega t + \theta) [J_1(\omega r) + aY_1(\omega r)]$$

$$H_y = \frac{1}{2}\sin(\omega t + \theta)\cos(\theta) [J_0(\omega r) - J_2(\omega r) + a(Y_0(\omega r) + Y_2(\omega r))] \\ -\frac{\sin(\theta)}{\omega r}\cos(\omega t + \theta) [J_1(\omega r) + aY_1(\omega r)]$$

where for the polar coordinates:  $r_1 < r < r_2$ ,  $r = \sqrt{x^2 + y^2}$ ,  $\theta = \arctan(y/x)$ .  $J_n$  and  $Y_n$  are the n-th order Bessel functions of the first and second kind, respectively. Due to the two cylinders are PEC, we have to enforce the boundary condition  $E_z = 0$  at  $r = r_1$  and  $r = r_2$ . The constants  $\omega$  and  $a$  are obtained by enforcing the boundary conditions on  $E_z$  at  $r = r_1$  and  $r = r_2$ . According to [Ditkowski et al., 2001], we set  $\omega = 9.813695999428405$  and  $a = 1.76368380110927$ .

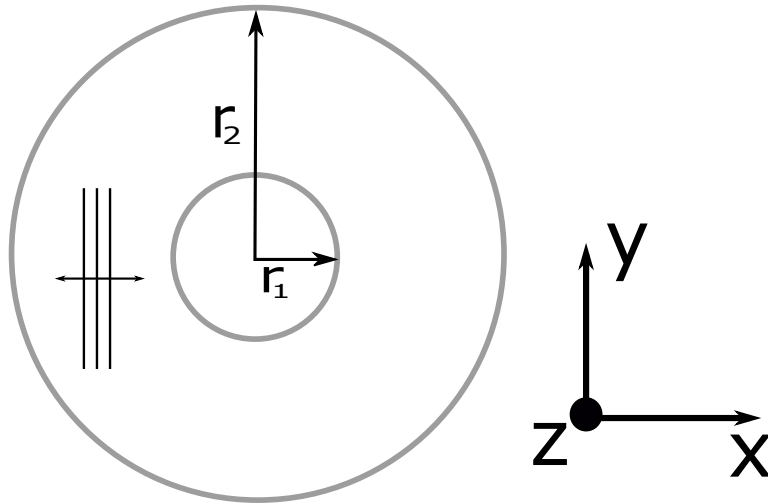


Figure 4.1: Concentric PEC cylinders resonator.

In this problem were considered two strategies: the first one is the general DGTD with straight side elements and the second one is the modified DGTD with CE. The simulations have been performed on three successively refined non-uniform grids whose characteristics are summarized in Table 4.1. For time integration has been used the LSERK4 method. Tables 4.2 and 4.3 show both the global  $L^2$  error and the convergence rate as a function of the mesh size, the time step for each mesh depending on the polynomial order and the number of degrees of freedom (DOF) for both DGTD with straight side elements and DGTD with CE, respectively. We use the same time step showed in Table 4.2 to obtain the results is Table 4.3. Finally, all errors were calculated at time  $t=0.333\text{ns}$ .

Fig 4.2 (a) and (b) illustrates respectively, the component  $E_z$  of the solution for the general DGTD and the modified DGTD into the mesh 1, using a polynomial order  $N = 5$ . As seen in Fig 4.2, the CE provides a better approximation of the boundaries than the straight side elements, even using a coarse mesh. Fig 4.3 shows the convergence rate for the global  $L^2$  error as a function of the number of DOF. This was made fixing the mesh 3 and varying the polynomial order. We selected the mesh 3 due to the discretization over the domain and especially in the boundaries is better than in the others meshes. Moreover, Fig. 4.3 shows that the general DGTD method becomes less efficient in terms of global  $L^2$  error as the number of DOF increases.

As can be seen in Table 4.2, the accuracy of the DGTD method with straight side elements is limited by the geometrical error, achieving convergence rates between 1.9 and 2. On the other hand, Table 4.3 shows that the geometrical error is mitigated using the CE. This modification allows us to obtain convergence rates up to two times higher in certain cases. By comparing all global  $L^2$  error values, it is clear that the DGTD method with CE provides a solution more accurately than the general DGTD. This is achieved using less elements and, consequently, less DOF.

Table 4.1: Characteristics of grids used for the concentric PEC cylinders resonator.

| Mesh               | M1 | M2 | M3  |
|--------------------|----|----|-----|
| Number of vertices | 28 | 41 | 113 |
| Number of elements | 36 | 58 | 182 |
| Number of CE       | 20 | 24 | 44  |

Table 4.2:  $L^2$  errors at time  $t=0.333\text{ns}$  and convergence rates for h-refinement using the general DGTD into the concentric PEC cylinders resonator problem.

| N | M1      | $\Delta t(\text{ps})$ | DOF | M2      | $\Delta t(\text{ps})$ | DOF  | M3      | $\Delta t(\text{ps})$ | DOF  | Rate |
|---|---------|-----------------------|-----|---------|-----------------------|------|---------|-----------------------|------|------|
| 2 | 2.07e-2 | 66.3                  | 216 | 1.35e-2 | 60.3                  | 348  | 2.30e-3 | 42.3                  | 1092 | 2.00 |
| 3 | 1.35e-2 | 44.6                  | 360 | 8.00e-3 | 40.6                  | 580  | 1.60e-3 | 28.33                 | 1820 | 1.94 |
| 4 | 1.24e-2 | 31.6                  | 540 | 7.90e-3 | 28.6                  | 870  | 1.50e-3 | 20                    | 2730 | 1.92 |
| 5 | 1.23e-2 | 23.3                  | 756 | 7.10e-3 | 21                    | 1218 | 1.50e-3 | 14.66                 | 3822 | 1.91 |

Table 4.3:  $L^2$  errors at time  $t=0.333\text{ns}$  and convergence rates for h-refinement using the modified DGTD with CE into the concentric PEC cylinders resonator problem.

| N | M1       | DOF | M2       | DOF  | M3       | DOF  | Rate |
|---|----------|-----|----------|------|----------|------|------|
| 2 | 3.17e-02 | 216 | 1.05e-02 | 348  | 6.66e-04 | 1092 | 3.51 |
| 3 | 2.20e-03 | 360 | 1.70e-03 | 580  | 2.70e-05 | 1820 | 4.00 |
| 4 | 2.23e-04 | 540 | 2.04e-04 | 870  | 3.80e-06 | 2730 | 3.7  |
| 5 | 1.80e-04 | 756 | 3.46e-05 | 1218 | 5.50e-07 | 3822 | 5.27 |

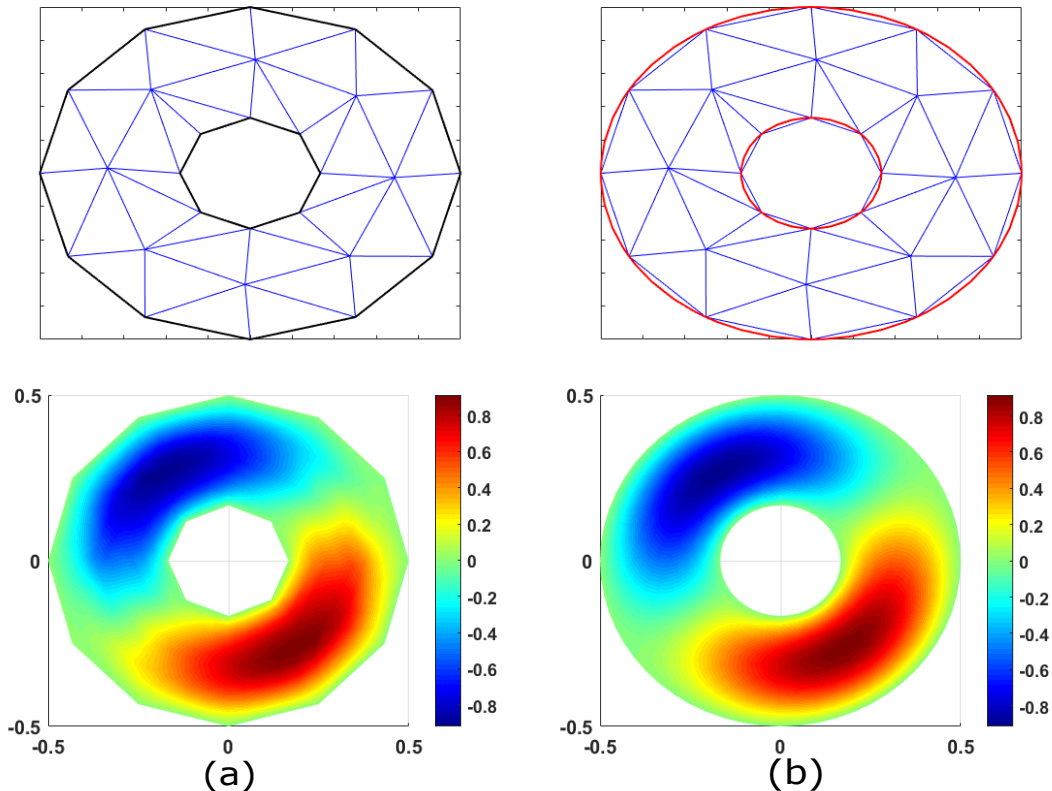


Figure 4.2: Triangular meshes and component  $E_z$  of the solution for the concentric PEC cylinders resonator at time  $t=0.333\text{ns}$ , using (a) straight side and (b) curved elements.



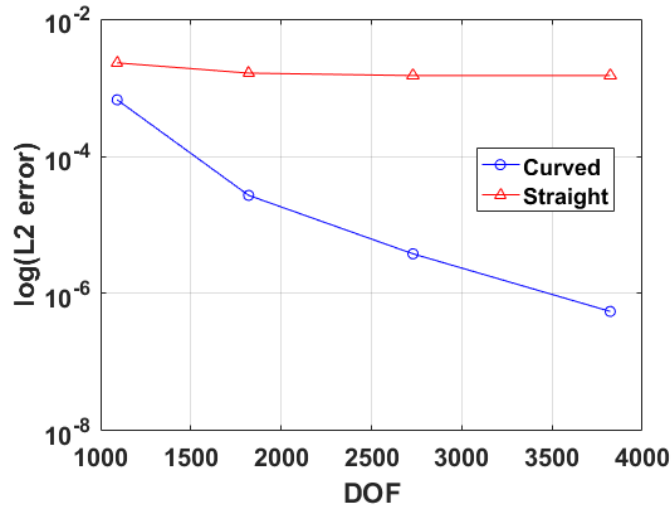


Figure 4.3: P-convergence for the concentric PEC cylinders resonator, using straight side and curved elements.

## 4.2 Scattering by a PEC circular cylinder

In this problem, we present the case when a plane wave with frequency  $f = 300$  MHz that propagates in the  $\hat{x}$  direction, impinges on a PEC circular cylinder. The incident field is imposed using the scattered field formulation. This problem can be formulated in 2D because the domain geometry has no variation in the  $\hat{z}$  direction. Fig 4.4 shows the geometry of the scenario. This test problem has been solved in many works, a clear example is [Balanis, 2012] where the expression of the analytical solution is detailed. So, we set  $\mu_r = \varepsilon_r = 1$  outside of cylinder and inside of it  $\sigma = \infty$ . The internal cylinder has a radius  $r = 0.5$  m. Furthermore, The computational domain  $\Omega$  is bounded by a square of side length  $\Omega_a = 2$  m centered at  $(0, 0)$ . For the boundary condition, we use a first order Silver-Muller. The simulations have been performed on three successively refined non-uniform grids whose characteristics are summarized in Table 4.4. For time integration has been used the LSERK4 method. The global  $L^2$  error of component  $E_z$  at  $t = 26.67ns$ , the time step for each mesh depending on the polynomial order, and the corresponding convergence rate are shown in Table 4.5 for straight side elements and Table 4.6 for CE. We use the same time step showed in Table 4.5 to obtain the results in Table 4.6. As in the previous problem, these values are calculated as a function of the mesh size and the number of DOF. It is important to say that each value with a (\*) is not taken into account for the convergence rate because is considered a larger error. Fig. 4.5 shows the component  $E_z$  of scattered field and spatial discretization of the elements in mesh 1, using a polynomial order  $N = 5$ . We choose the poorest mesh to show that it is possible to reproduce a curved boundary with accuracy using CE and a

higher polynomial order. Fig 4.6 shows the convergence rate for the global  $L^2$  error as a function of the number of DOF. This was made again fixing the mesh 3 and varying the polynomial order. For this problem, the x-wise distribution of the scattered field  $E_z$  was plotted for  $y = 0$  and it is shown in Fig. 4.7. Moreover, this figure illustrates that the CE scheme provides a better approximation in relation with the analytical solution than the straight side elements. It is clear from data in Table 4.5 that the solution accuracy for high degree  $N$  is limited by the geometrical error when we use straight side elements. By comparing all global  $L^2$  error values into Tables 4.5 and 4.6, one can notice that to achieve a given accuracy, the meshes with CE require less DOF than the meshes with straight side elements. For instance, for an accuracy of  $10^{-2}$ , we can save around 50% to 90% of DOF. For the convergence analysis, it can be seen that we achieved larger convergence rates using CE than straight side elements, similar as the previous problem. As can be seen in Tables 4.5 and 4.6, the converge rate was low comparing with the previous problem, this can be happen due to the error induced by the SMA boundary condition. This can be solved using a PML as boundary condition.

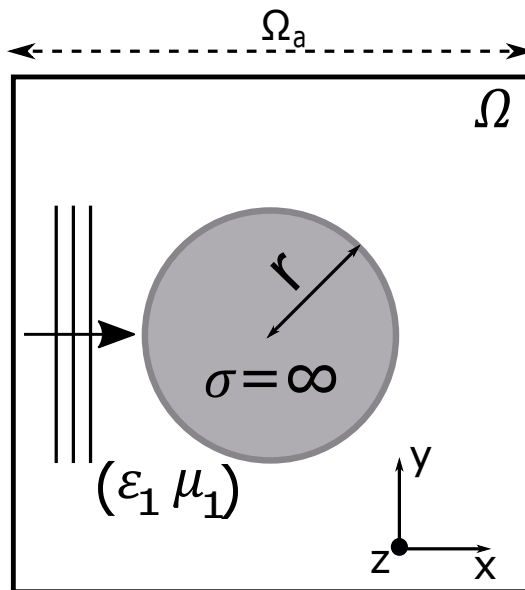


Figure 4.4: Uniform plane wave illuminating a PEC circular cylinder.

Table 4.4: Characteristics of the grids used for the scattering by a PEC circular cylinder.

| Mesh               | M1 | M2  | M3  |
|--------------------|----|-----|-----|
| Number of vertices | 44 | 138 | 439 |
| Number of elements | 60 | 220 | 765 |
| Number of CE       | 8  | 16  | 33  |

Table 4.5:  $L^2$  errors at time  $t=26.67\text{ns}$  and convergence rates for h-refinement using the general DGTD into the scattering by a PEC circular cylinder problem.

| N | M1                 | $\Delta t(\text{ps})$ | DOF  | M2               | $\Delta t(\text{ps})$ | DOF  | M3               | $\Delta t(\text{ps})$ | DOF   | Rate |
|---|--------------------|-----------------------|------|------------------|-----------------------|------|------------------|-----------------------|-------|------|
| 2 | $1.60\text{e-}1^*$ | 159                   | 360  | $1.10\text{e-}1$ | 76.3                  | 1320 | $7.80\text{e-}2$ | 35                    | 4590  | 0.50 |
| 3 | $1.50\text{e-}1^*$ | 107                   | 600  | $1.07\text{e-}1$ | 51.3                  | 2200 | $5.20\text{e-}2$ | 23.3                  | 7650  | 1.00 |
| 4 | $1.50\text{e-}1^*$ | 75.3                  | 900  | $1.06\text{e-}1$ | 36.3                  | 3300 | $4.12\text{e-}2$ | 16.6                  | 11475 | 1.37 |
| 5 | $1.50\text{e-}1^*$ | 55.6                  | 1260 | $1.05\text{e-}1$ | 26.6                  | 4620 | $3.82\text{e-}2$ | 12.3                  | 16065 | 1.45 |

Table 4.6:  $L^2$  errors at time  $t=26.67\text{ns}$  and convergence rates for h-refinement using the modified DGTD with CE into the scattering by a PEC circular cylinder problem.

| N | M1                | DOF  | M2                | DOF  | M3                | DOF   | Rate |
|---|-------------------|------|-------------------|------|-------------------|-------|------|
| 2 | $1.08\text{e-}01$ | 360  | $4.70\text{e-}02$ | 1320 | $1.90\text{e-}02$ | 4590  | 1.25 |
| 3 | $9.67\text{e-}02$ | 600  | $4.01\text{e-}02$ | 2200 | $1.01\text{e-}02$ | 7650  | 1.63 |
| 4 | $8.34\text{e-}02$ | 900  | $3.50\text{e-}02$ | 3300 | $8.00\text{e-}03$ | 11475 | 1.70 |
| 5 | $7.11\text{e-}02$ | 1260 | $3.01\text{e-}02$ | 4620 | $7.00\text{e-}03$ | 16065 | 1.67 |

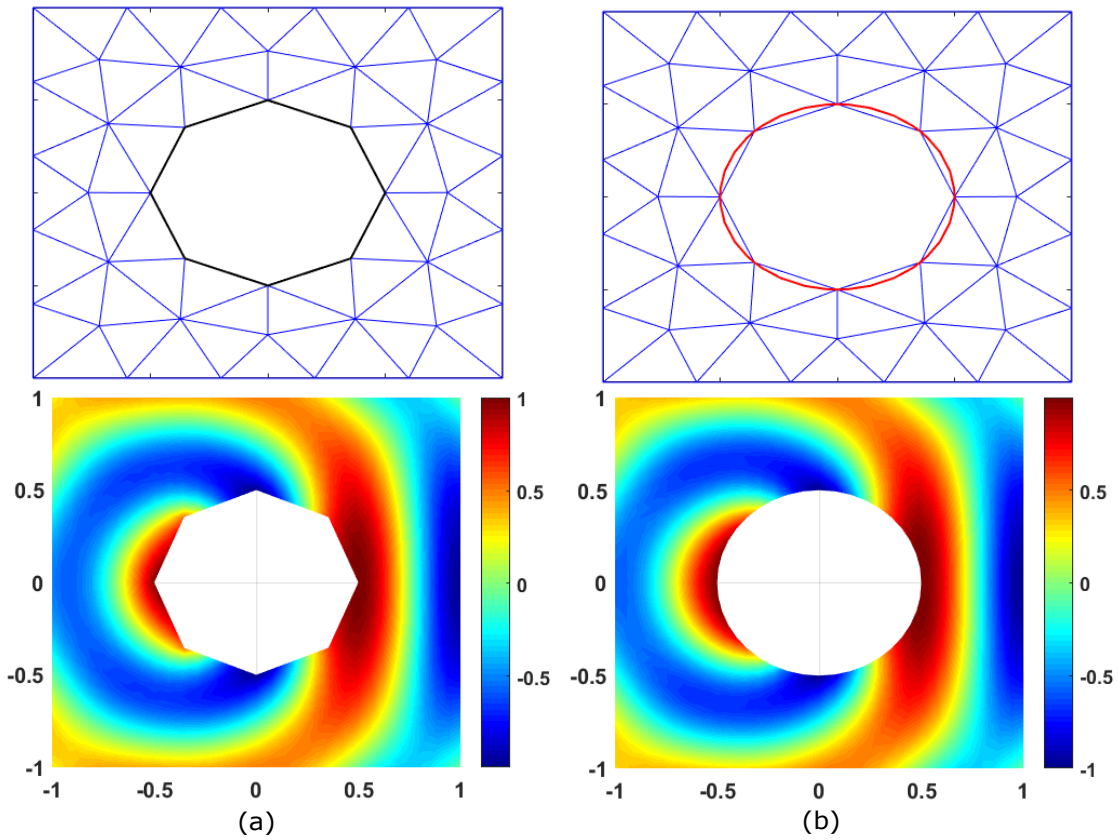


Figure 4.5: Scattered field by a PEC circular cylinder using (a) straight side and (b) curved elements for the mesh 1.

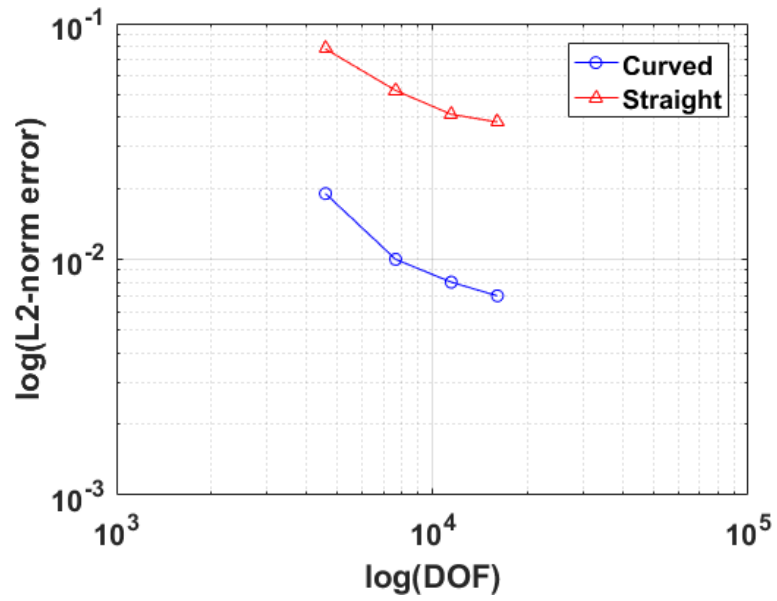


Figure 4.6: P-convergence for the scattered field by a PEC circular cylinder problem, using straight side and curved elements.

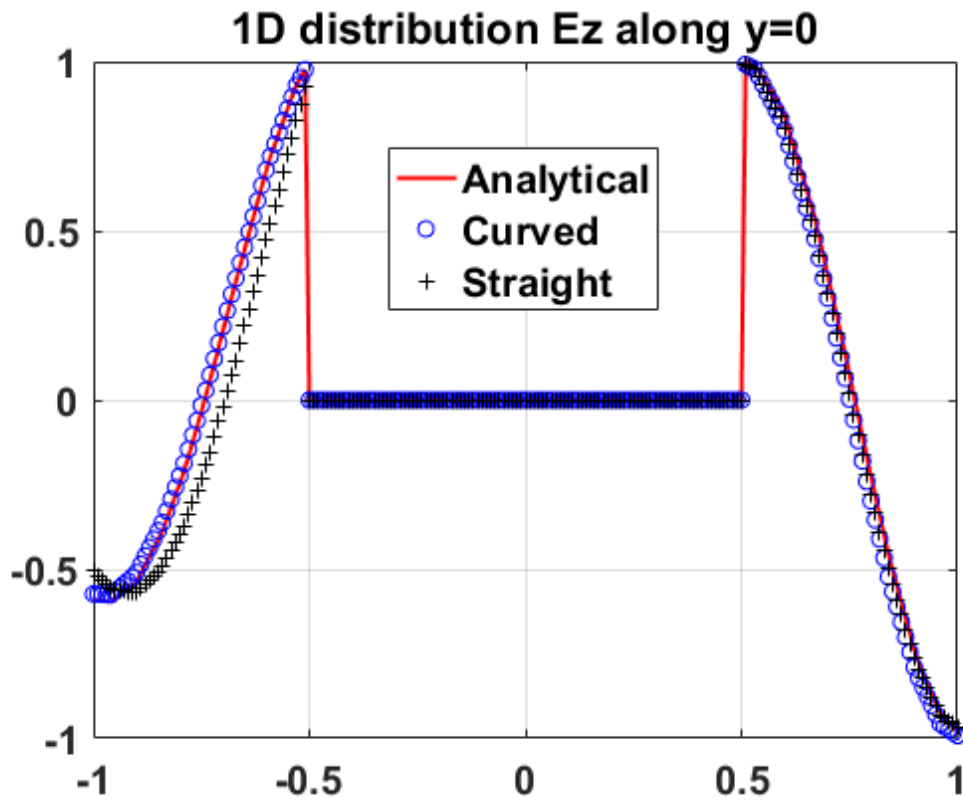


Figure 4.7: x-wise 1D distribution of the solution of the scattered field by a PEC circular cylinder for straight side and curved elements.

### 4.3 Scattering by a dielectric circular cylinder

In this problem a dielectric circular cylinder is illuminated by a plane wave with frequency  $f = 300$  MHz, experiencing reflection and refraction at the material interface. The incident field is imposed using the scattered field formulation. The scenario is shown in Fig. 4.8. This problem has been considered in various works as [Cai and Deng, 2003] and its analytical solution is found in [Jin, 2015]. We consider a non-magnetic material, therefore,  $\mu_{r_2} = 1$  and the material exterior to the cylinder is assumed to be vacuum  $\mu_{r_1} = \varepsilon_{r_1} = 1$ . The internal cylinder has a radius of  $r = 0.6$  m and is filled with a material of relative permittivity  $\varepsilon_{r_2} = 2.0$ . The computational domain  $\Omega$  is bounded by a square of side length  $\Omega_a = 2$  m centered at  $(0,0)$ . A first order Silver-Muller absorbing condition is applied on the boundary of the square domain. The simulations have been performed on three successively refined non-uniform grids whose characteristics are summarized in Table 4.7. For time integration has been used the LSERK4 method. Moreover, Tables 4.8 and 4.9 show the global  $L^2$  error of the component  $E_z$  for straight and CE at time  $t = 26.67ns$ , the time step for each mesh depending on the polynomial order. Also, these tables show the convergence rate for the two cases. We use the same time step showed in Table 4.8 to obtain the results in Table 4.9. These values are calculated as a function of the mesh size and the number of DOF. The symbol (\*) means that the value is not taken into account for the convergence rate, similar as in the previous problem. Fig. 4.9 shows the component  $E_z$  of the scattered field at  $t = 26.67ns$  in the mesh 1 with a polynomial order  $N = 5$ . It can be seen that CE provides a better approach on the curved boundary, even using the poorest mesh. At first glance, both solutions look very similar, however, as described in Tables 4.8 and 4.9, CEs provide a more accurate approximation, achieving an accuracy of  $10^{-3}$  that is not possible to obtain with the straight side elements under these conditions. Fig 4.10 shows the convergence rate for the global  $L^2$  error as a function of the number of DOF. Again, we fixing the mesh 3 and varying the polynomial order. This figure shows that the CE scheme becomes more efficient than the general DGTD, in terms of global  $L^2$  error as the order of approximation  $N$  increases. Fig. 4.11 illustrates the field distribution of  $E_z$  through the  $x$  axis when  $y = 0$ .

Table 4.7: Grids used for the scattering by a dielectric circular cylinder.

| Mesh               | M1 | M2  | M3   |
|--------------------|----|-----|------|
| Number of vertices | 55 | 165 | 567  |
| Number of elements | 88 | 288 | 1052 |
| Number of CE       | 24 | 40  | 80   |

Table 4.8:  $L^2$  errors at time  $t=26.67\text{ns}$  and convergence rates for h-refinement using the general DGTD into the scattering by a dielectric circular cylinder problem.

| N | M1                 | $\Delta t(\text{ps})$ | DOF  | M2               | $\Delta t(\text{ps})$ | DOF  | M3               | $\Delta t(\text{ps})$ | DOF   | Rate  |
|---|--------------------|-----------------------|------|------------------|-----------------------|------|------------------|-----------------------|-------|-------|
| 2 | $2.10\text{e-}1^*$ | 122                   | 528  | $7.23\text{e-}2$ | 75                    | 1728 | $3.40\text{e-}2$ | 38                    | 6312  | 1.08  |
| 3 | $9.72\text{e-}2$   | 82                    | 880  | $5.23\text{e-}2$ | 50                    | 2880 | $1.92\text{e-}2$ | 25                    | 10520 | 1.17  |
| 4 | $8.37\text{e-}2$   | 58                    | 1320 | $4.81\text{e-}2$ | 35                    | 4320 | $1.64\text{e-}2$ | 18                    | 15780 | 1.175 |
| 5 | $6.89\text{e-}2$   | 43                    | 1848 | $3.90\text{e-}2$ | 26                    | 6048 | $1.06\text{e-}2$ | 13                    | 22092 | 1.35  |

Table 4.9:  $L^2$  errors at time  $t=26.67\text{ns}$  and convergence rates for h-refinement using the modified DGTD with CE into the scattering by a dielectric circular cylinder problem.

| N | M1                | DOF  | M2                | DOF  | M3                | DOF   | Rate |
|---|-------------------|------|-------------------|------|-------------------|-------|------|
| 2 | $1.10\text{e-}01$ | 528  | $3.48\text{e-}02$ | 1728 | $2.30\text{e-}02$ | 6312  | 1.12 |
| 3 | $4.45\text{e-}02$ | 880  | $2.96\text{e-}02$ | 2880 | $7.00\text{e-}03$ | 10520 | 1.33 |
| 4 | $4.33\text{e-}02$ | 1320 | $2.60\text{e-}02$ | 4320 | $3.80\text{e-}03$ | 15780 | 1.75 |
| 5 | $3.36\text{e-}02$ | 1848 | $2.42\text{e-}02$ | 6048 | $1.90\text{e-}03$ | 22092 | 2.07 |

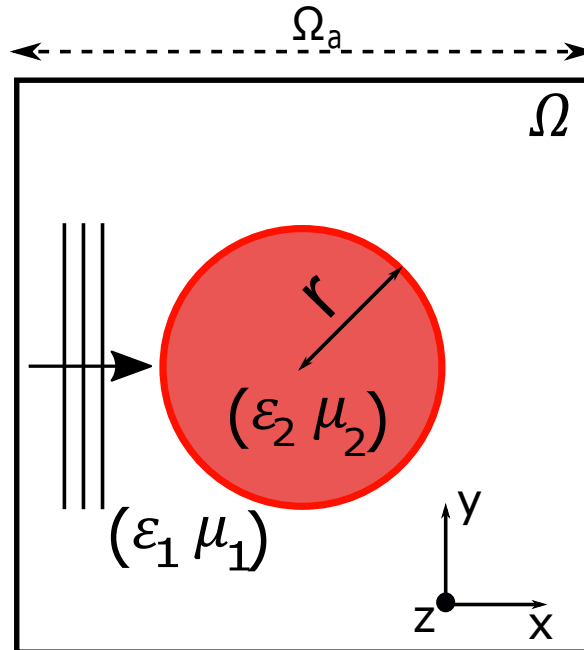


Figure 4.8: Uniform plane wave illuminating a dielectric circular cylinder.

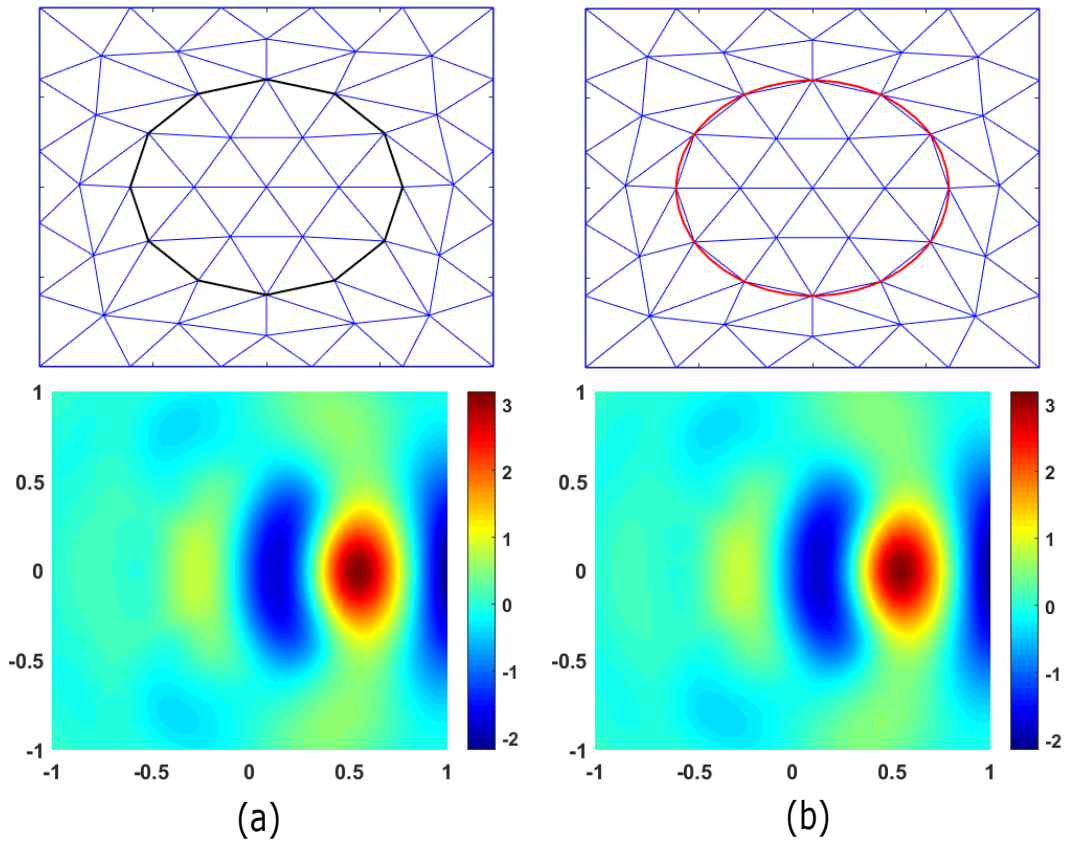


Figure 4.9: Scattered field by a dielectric circular cylinder using (a) straight side and (b) curved elements for the mesh 1.

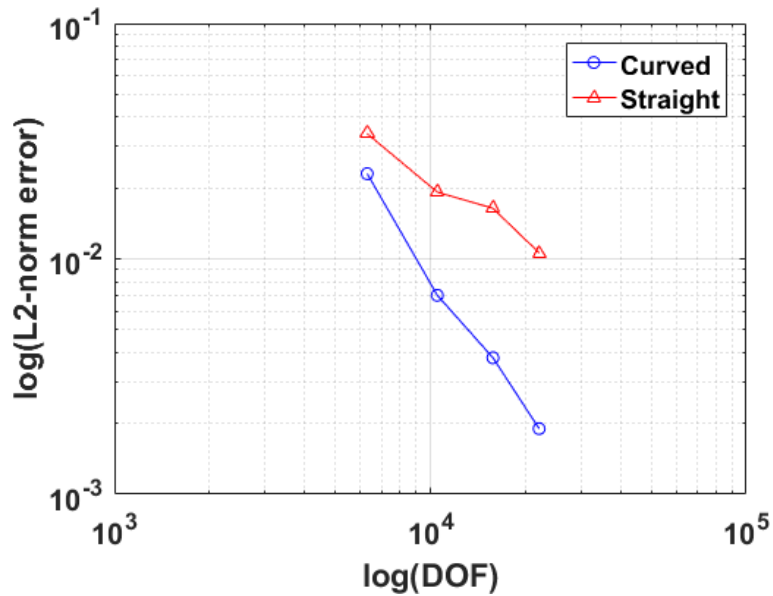


Figure 4.10: P-convergence for the scattered field by a dielectric circular cylinder problem, using straight side and curved elements.

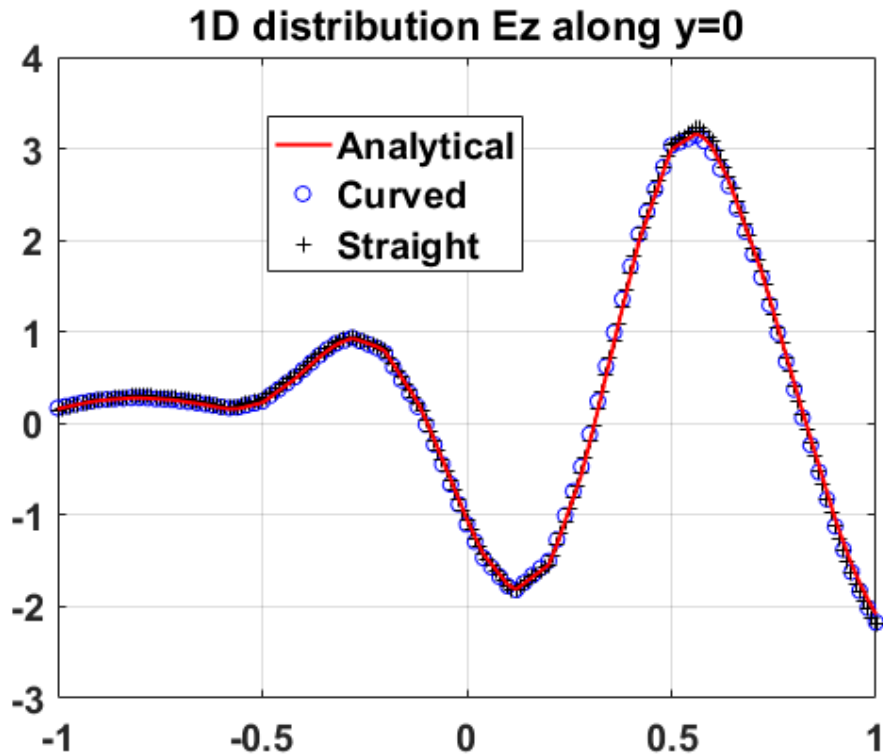


Figure 4.11: x-wise 1D distribution of the solution of the scattered field by a dielectric circular cylinder for straight side and curved elements at time  $t=26.67\text{ns}$ .

#### 4.4 Scattering by a PEC coated circular cylinder

In order to show the behavior of the DGTD with curved elements in more complex problems, we choose to study the scattering by a PEC coated cylinder. Many research has been conducted on the problem of coated conducting cylinders due to their importance in many applications. One of them is the protection of objects from radar illumination, where the coating can be used to obtain the maximum reduction of the radar dispersion cross section. This problem was solved for the first time by [Tang, 1957]. In that work he showed an exact series solution by using cylindrical eigenfunctions expansion. The geometry of the problem is depicted in Fig. 4.12, where can be seen a cross-sectional view of a coated PEC cylinder assumed to be infinitely long in the  $\hat{z}$  direction. The computational domain  $\Omega$  is bounded by a square of side length  $\Omega_a = 4$  m centered at  $(0, 0)$ . For the boundary condition, we use a first order Silver-Muller. The region outside of the cylinder are assumed to be vacuum  $\mu_{r_1} = \varepsilon_{r_1} = 1$ . The material of the coating region is assumed to be linear and isotropic with permittivity  $\varepsilon_{r_2} = 2.25$  and  $\mu_{r_2} = 1$ . The internal PEC cylinder has a radius of  $r_1 = 0.5\text{m}$  and the external coated cylinder has a radius of  $r_2 = 0.8\text{m}$ . The frequency of the incident plane



wave is  $f = 300$  MHz. Table 4.10 shows the comparison between the meshes used in this problem and the global  $L^2$  error, for both straight element and curved element. For time integration has been used the LSERK4 method. Also, in this problem, the time step used by CE is decreased by 30% compared to SSE. Fig. 4.13 shows the component  $E_z$  of the scattered field along the axis  $x$  for  $y = 0$ . Fig. 4.14 shows the component  $E_z$  of the scattered and total field at  $t = 26.67ns$ . As can be seen in Table 4.10, the meshes are different for both cases because the objective was showing that a smaller quantity of elements in the modified DGTD allows obtaining a more precise solution. Therefore, in analysing Fig. 4.13 and Table 4.10, we can conclude that CE provides a better approximation of the solution, saving around 70% of elements and 50% of DOF.

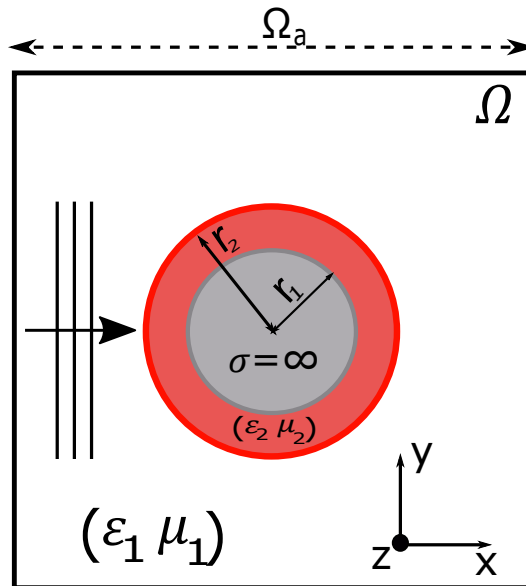


Figure 4.12: Uniform plane wave illuminating a PEC coated circular cylinder.

Table 4.10: Characteristics of grids used for the scattering by a PEC coated circular cylinder.

|                    | Mesh with straight side elements | Mesh with CE |
|--------------------|----------------------------------|--------------|
| N                  | 3                                | 4            |
| Number of vertices | 1702                             | 558          |
| Number of elements | 3254                             | 1034         |
| DOF                | 32540                            | 15510        |
| Number of CE       | 0                                | 88           |
| Global $L^2$ error | 7.1e-03                          | 4.8e-03      |
| Time step (ps)     | 27.3                             | 35.6         |

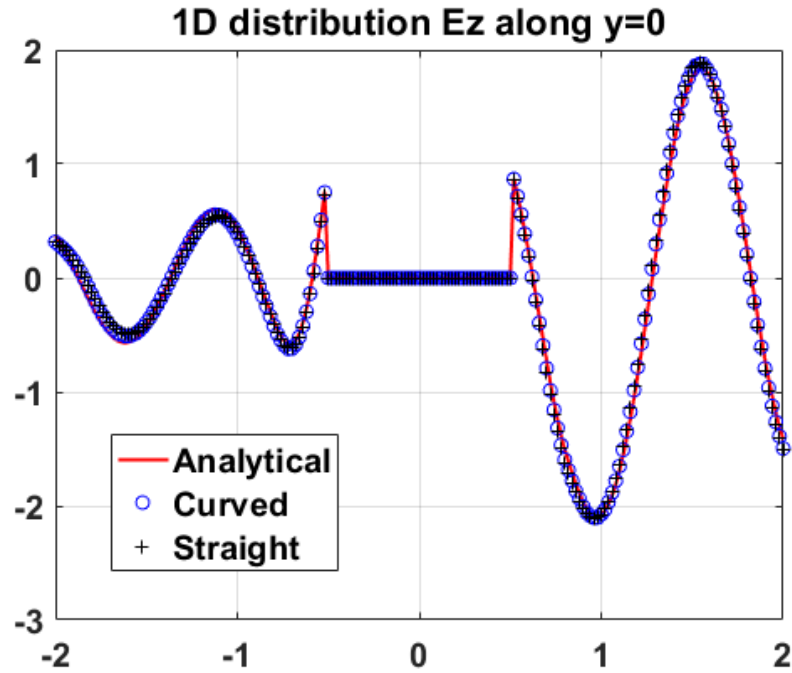


Figure 4.13: x-wise 1D distribution of the solution of the scattered field by a PEC coated circular cylinder for straight side and curved elements at time  $t=26.67\text{ns}$ .

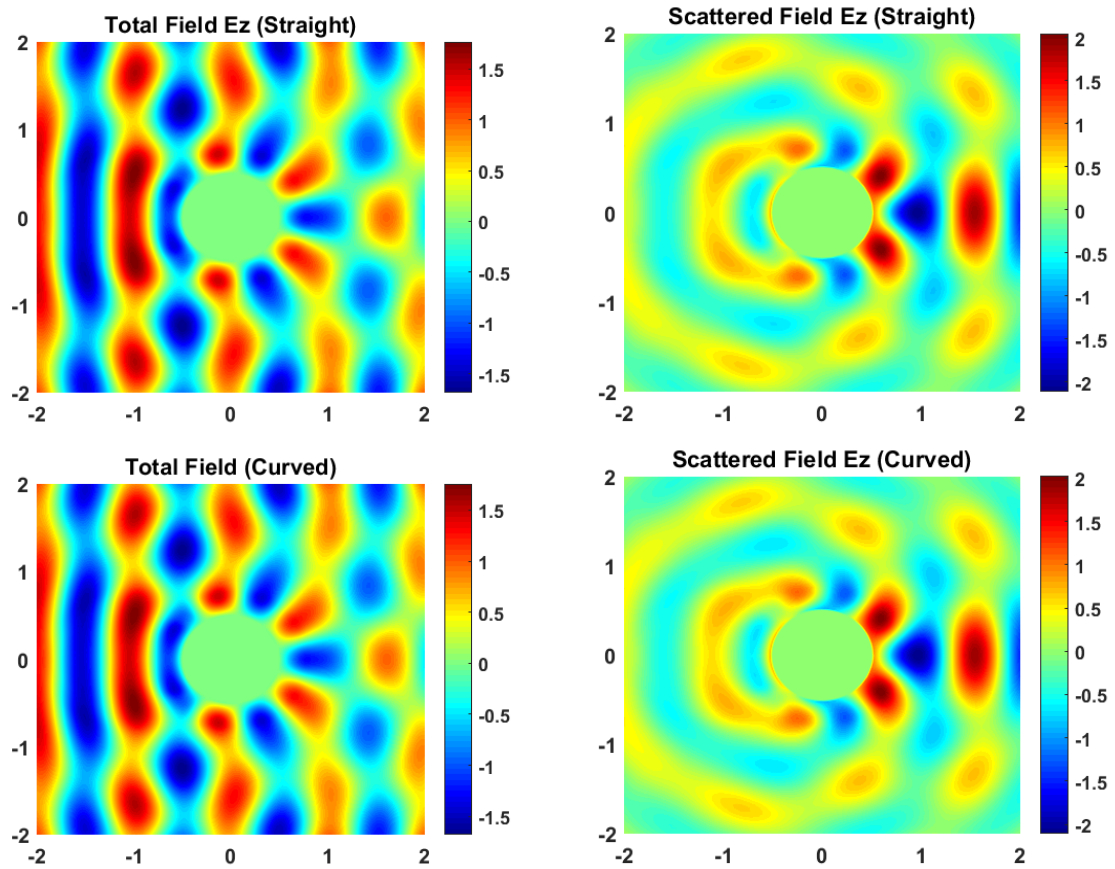


Figure 4.14: Total and Scattered field by a PEC coated circular cylinder at time  $t=26.67\text{ns}$ , using straight side and curved elements

## 4.5 L-shaped photonic crystal guide

As can be seen in the previous problems, the implementation of the CE in DGTD method has a lot of advantages in terms of decreasing the number of elements and consequently, decreasing the number of DOF. All this without compromising the precision of the solution. However, these problems have a very small number of CE in comparison with real engineering problems as photonic crystal, where the number of scatters is much higher. Therefore, we choose the L-shaped photonic guide in order to evaluate the behavior of this scheme in large structures. The photonic crystal characterization is based on the construction of band diagrams. These structures can be studied if we know their symmetry properties, that is, we can understand the electromagnetic properties of the system only knowing the symmetry properties.

Basically, a bidimensional (2-D) photonic crystal consists of a square lattice of parallel infinite dielectric rods in air. This structure can be seen in Fig. 4.15, where  $\mathbf{a}$  is the lattice constant and  $r_a$  is the radius of the scatters. In Fig. 4.15, we consider a system with continuous translational symmetry in the  $\hat{z}$  direction, that is, the system is invariant under any translation in a given direction. On the other hand, for the plane  $xy$ , the system has discrete translational symmetry, that means, the structure is invariant to a translation over a distance that is multiple of a certain length. According to Fig 4.15, the basic photonic crystal structure is filled with scatters separately by a constant distance. However, it is necessary to insert the so-called defects in the crystal lattice to build some engineering applications. For instance, the characteristics of the photonic crystal can be altered in Fig 4.15, removing or changing the characteristics of a dielectric column, creating waveguides that could be based on other devices such as logic gates [Fu et al., 2013]. Finally, applying some defects in the previous structure, we construct the same L-shaped photonic crystal guide used in [de Souza et al., 2019], see Fig 4.16. The lattice constant  $\mathbf{a} = 0.57\mu m$  and the rods are assumed to have a circular cross-section of radius  $r_a = 0.114\mu m$ . The dielectric is chosen to have a refractive index  $\eta \approx 3.4$  ( $\varepsilon_r = 11.5$ ), appropriate for Silicon (Si). This crystal has a complete band gap for TM polarization between frequencies 0.35 and 0.42 ( $\omega\mathbf{a}/2\pi c$ ). The incident pulse is placed in the left input of the waveguide and is given by:

$$E_z(x, y, t) = E_0 \cos\left(\frac{\pi y}{d}\right) \cos(2\pi f_m t) e^{-\left(\frac{t-t_0}{2\sigma}\right)^2} \quad (4.3)$$

where  $d = 2(\mathbf{a} - r_a)$  is the waveguide length,  $\sigma_{BW} = 5 \times 10^{-14}$  s is a parameter which define the pulse bandwidth,  $f_m = 2 \times 10^{14}$  Hz is the central frequency and  $t_0 = 2.5 \times 10^{-13}$  s.

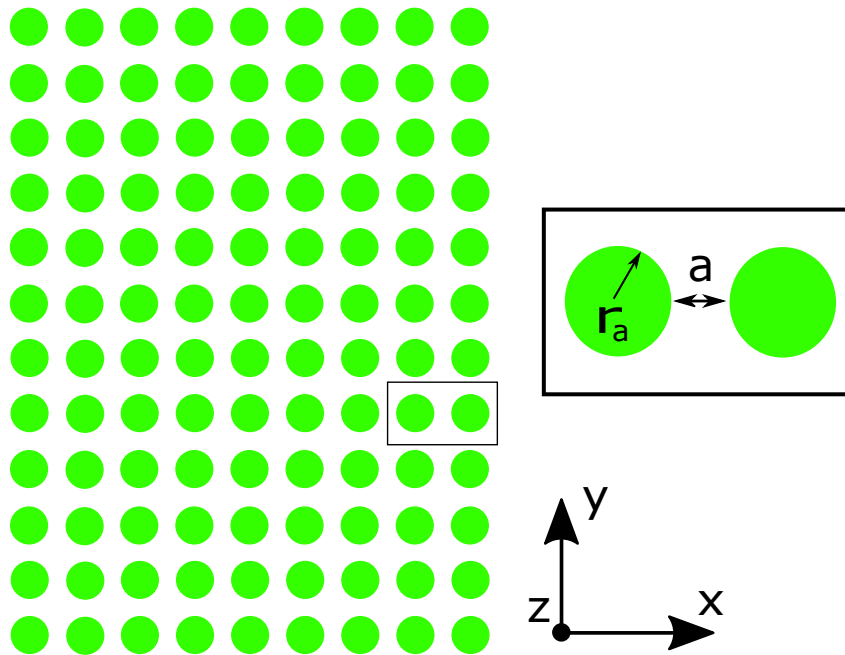


Figure 4.15: Photonic crystal structure.

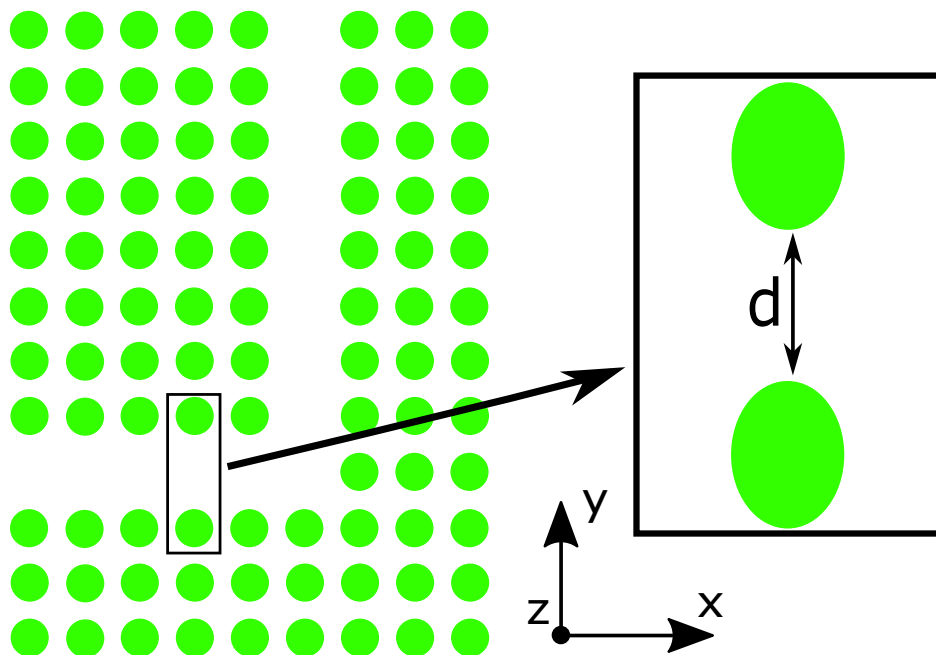


Figure 4.16: L-shaped photonic crystal guide.

In Fig 4.17 and 4.18, the computational domain represented by a triangular mesh and the solution for the component  $E_z$  are shown, for straight side and curved elements, respectively. A first order Silver-Muller absorbing condition is applied on the boundary of the computational domain. Table 4.11 shows the characteristics of each mesh used on both the straight side and the curved elements.

Table 4.11: Meshes used to represent the L-shaped photonic guide.

|                    | Mesh with<br>straight side elements | Mesh with CE |
|--------------------|-------------------------------------|--------------|
| N                  | 3                                   | 2            |
| Number of vertices | 5735                                | 3944         |
| Number of elements | 11294                               | 7680         |
| DOF                | 112940                              | 46080        |
| Number of CE       | 0                                   | 1504         |
| Time step (ps)     | 5                                   | 1.5          |

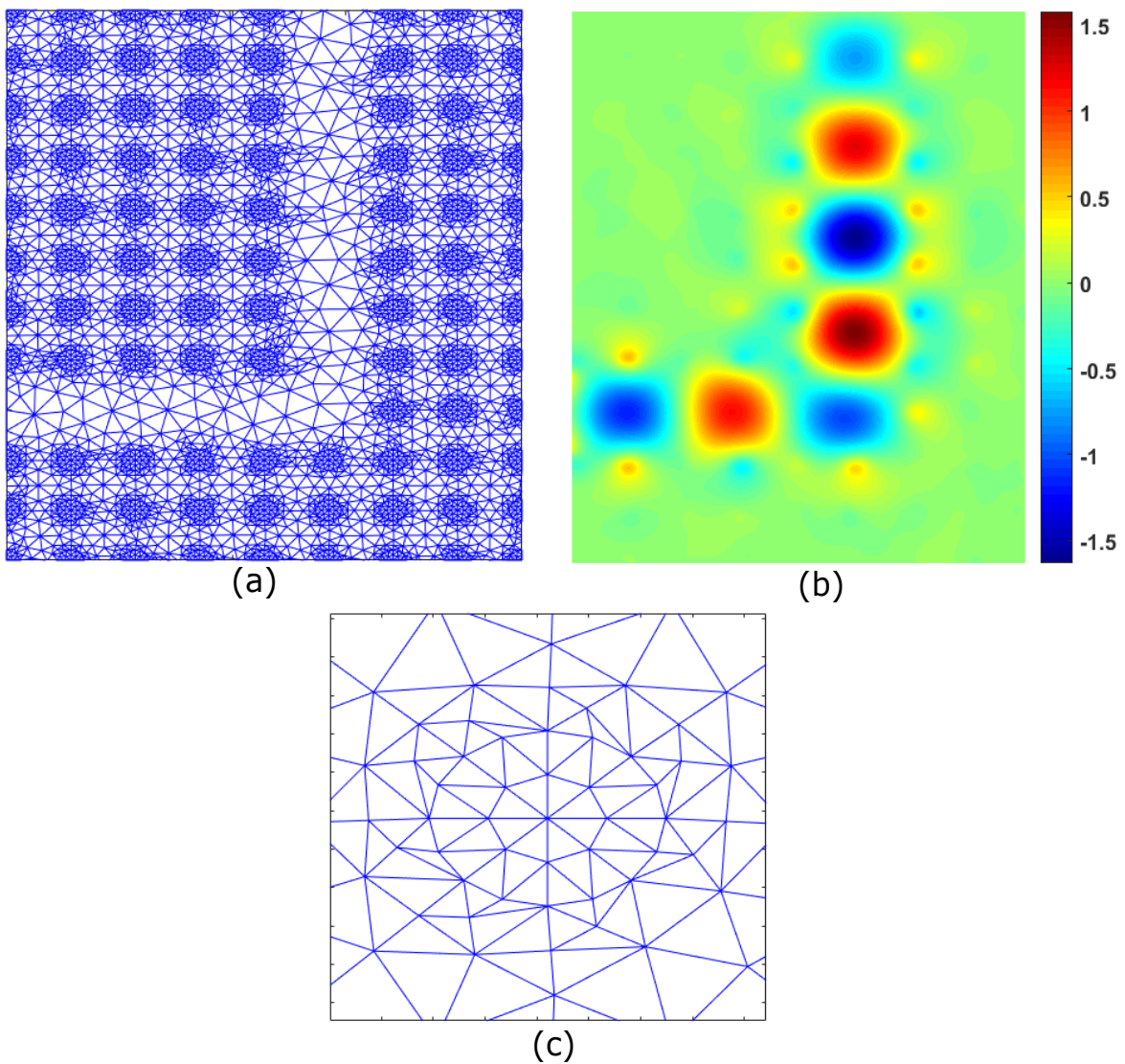


Figure 4.17: L-shaped photonic crystal guide, (a) computational domain represented by a refined triangular mesh, (b) Component  $E_z$  of solution, (c) dielectric scatterer represented by small straight side elements.

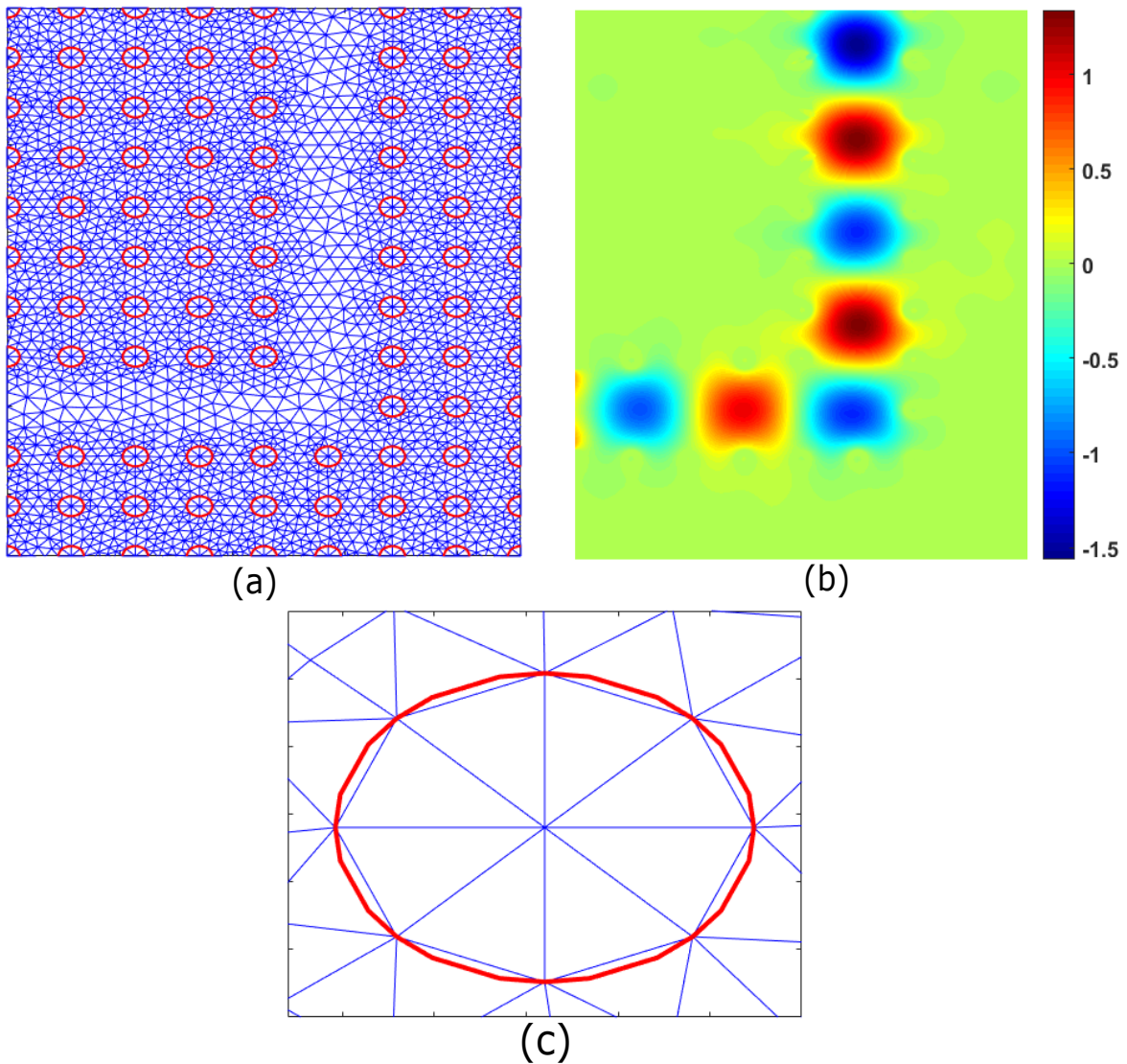


Figure 4.18: L-shaped photonic crystal guide, (a) computational domain represented by a triangular mesh, (b) Component  $E_z$  of solution, (c) dielectric scatterer represented by curved elements.

Fig. 4.17 (b) shows the component  $E_z$  of the solution, it can be seen that part of the field is confined in the adjacent scatters while the pulse is propagating, this may be due to numerical error or an induced error by the geometry of the scatters. On the contrary, it can be seen in Fig. 4.18 (b) that this problem disappears, showing a more defined solution. Moreover, as can be seen in Fig. 4.17 (c), we have to apply a h-refinement to guarantee the circular shape of each dielectric scatterer, that means the number of elements in each dielectric scatterer is increased by four times. On the other hand, in Fig. 4.18 (c), the number of elements has been maintained in each scatterer and the curved elements scheme has been applied in each one. Therefore, we have a better

approximation of each curved boundary using less elements but as a consequence, the pre-processing time is increased. At first glance, it is clear that the DGTD method with curved elements provides a better solution. However, in these types of problems that do not have an analytical solution, it is difficult to compare both solutions. An interesting option to compare both solutions could be to know the dispersion caused by the waveguide on the propagated pulse. Consequently, a field detector was placed in the output of the waveguide. Finally, a Fast Fourier transform (FFT) is calculated from the data obtained from the pulses in the time domain. Fig. 4.19 shows a comparison of the FFT for the signal obtained for straight side case and curved case. Table 4.12 show the results in terms of the dispersion caused by the waveguide on the signals.

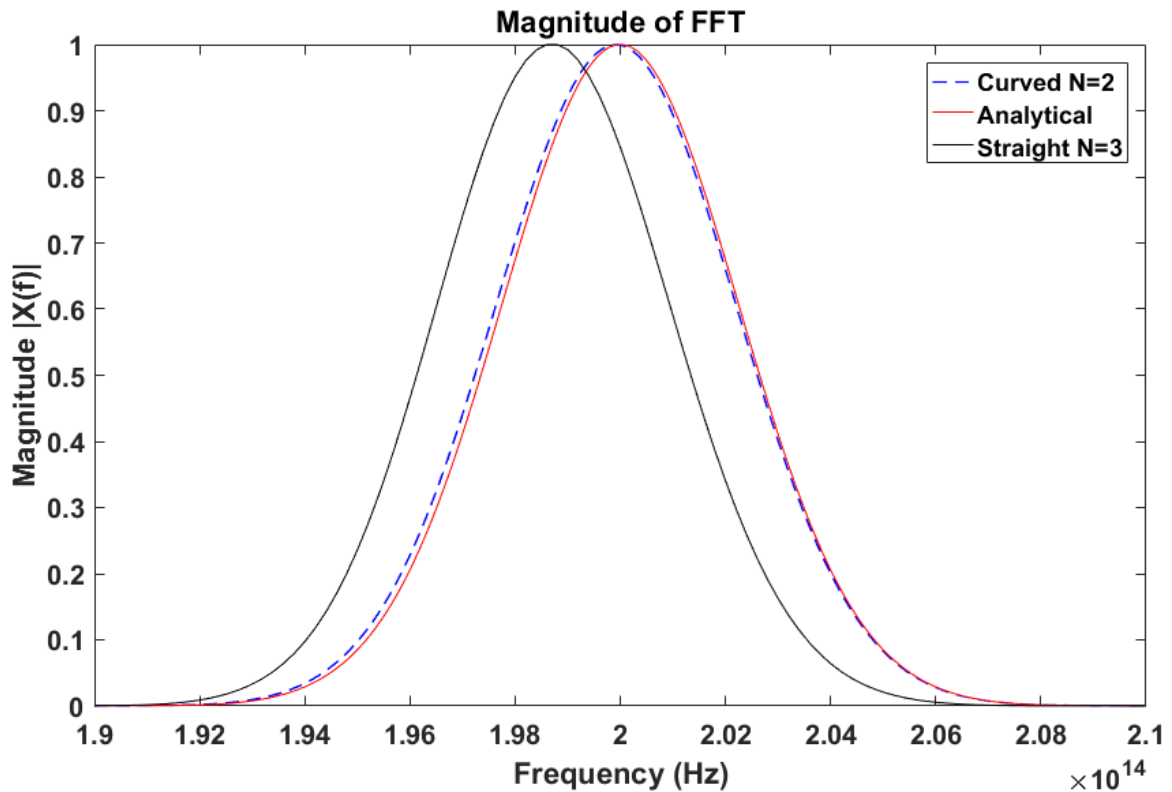


Figure 4.19: FFT of the signals propagated inside the waveguide.

Table 4.12: Central frequencies for each pulses.

| Solution               | Central frequency (Hz) |
|------------------------|------------------------|
| Analytical             | $2 \times 10^{14}$     |
| Straight side elements | $1.988 \times 10^{14}$ |
| Curved elements        | $1.999 \times 10^{14}$ |

As can be seen in Table 4.12, the dispersion caused by the waveguide using straight side elements was 0.6% in relation to the central frequency. On the other hand, using curved elements the dispersion in relation with central frequency was 0.05%, that is, the dispersion decreased more than 90% in the propagated pulse using CE. Moreover, according to Table 4.11 these results were obtained saving more than 30% of elements and 60% of DOF. Also, for this problem, it was necessary to use a slightly lower time step for CE than for SSE elements as can be seen in Table 4.11. It occurs because the CE scheme has instability problems when large problems are analyzed.



# Chapter 5

## Conclusions

This work addressed a complete analysis of the DGTD method with curved elements to solve (2D) electromagnetic problems. In order to achieve this, we presented step by step the whole scheme for the DGTD method with straight side elements, this was essential to understand how the method works and as a result, implementing the modifications for the curved element scheme. The obtained results demonstrated that the CE scheme makes possible a better approximation without increase computational effort, due to the curved boundaries are represented accurately using few elements. In this regard, it is important to clarify that the curved element scheme demands a higher pre-processing computational time to build the element matrices for each CE and also, it is required to evaluate each CE separately in the loop time, because the jacobian is not constant in each CE. However, those efforts are rewarded in terms of accuracy and decreasing the amount of elements necessary to represent a curved surface.

In the first problem of the concentric PEC cylinders resonator, we presented an analysis in terms of global  $L^2$  error and convergence rate with the purpose of validating our method. These results showed that for a very common problem used in the literature to test the CE scheme, the DGTD with CE method provides convergence rates of up to 5, which would be impossible to obtain in other very common methods such as FDTD or FEMTD. Now, for the next two very common electromagnetic scattering problems (scattering by a PEC and dielectric circular cylinders) can be seen that the CE scheme provides a better approximation of the solution in terms of global  $L^2$  error even if the domain was well discretized or not.

Once the method has been validated, we had to find a more complex problem to evaluate the behavior of the scheme. Therefore, we chose the PEC coated circular cylinder, this problem is very interesting because different from the previous cases, two scatters must be considered. Moreover, this problem will need a higher quantity of CE

to represent the two scatters. As a result, we found again that the CE scheme provides better results than the straight side scheme, using fewer elements and consequently, decreasing the number of DOF.

From the application of the CE scheme in the scattering problems and the possibility to work with more than one scatter, we decided to solve a very complex engineering problem. In this case, we selected the L-shaped photonic guide problem studied in [de Souza et al., 2019]. This problem is very interesting for us because a photonic crystal is based on many dielectric circular scatters. The results with the CE scheme were satisfactory and allowed us to obtain a better approximation of the solution with a dramatic decrease in the number of elements and DOF. Then, it is possible to conclude that the implementation of the DGTD method with CE provides a very powerful numerical technique due to the geometrical error caused by the bad approximation over the curved boundaries is eliminated.

## 5.1 Futures works

The development of this work allowed us to know some flaws in the DGTD method with CE that can be studied in detail. Thus, the futures works proposals are related mainly with the following ideas:

- As presented throughout the text, the nodes discretization is made depending on the polynomial order. Therefore, all the elements maintain the same quantity of nodes, including CE. One interesting option could be implementing a p-refinement in the straight side elements. This means maintaining the accuracy of CE and in addition, decreasing the computational effort.
- To perform an analysis of the stability of the method when the CE scheme is implemented, because when we use a higher polynomial order in a large scale problem, it is necessary to decrease the time step.
- According to the previous suggestions, we could apply the LTS as in [de Souza et al., 2019] to guarantee the stability of the method and also, as was shown in that work, optimizing the computational time.
- Finally, this work showed that the CE scheme in the DGTD method presents significative improvement in terms of accuracy. However, the fact that all the test are bidimensional imposes a restriction in terms of applications over more realistic problems. Hence, a 3D scheme with CE for the DGTD method is very necessary.

# Bibliography

- Ainsworth, M., Monk, P., and Muniz, W. (2006). Dispersive and dissipative properties of discontinuous galerkin finite element methods for the second-order wave equation. *Journal of Scientific Computing*, 27(1-3):5–40.
- Alvarez, J., Angulo, L., Bretones, A. R., and Garcia, S. G. (2012). A spurious-free discontinuous galerkin time-domain method for the accurate modeling of microwave filters. *IEEE transactions on microwave theory and techniques*, 60(8):2359–2369.
- Alvarez, J., Angulo, L. D., Bretones, A. R., van Coevorden, C. M. d. J., and Garcia, S. G. (2015). Efficient antenna modeling by dgtd: Leap-frog discontinuous galerkin timedomain method. *IEEE Antennas and Propagation Magazine*, 57(3):95–106.
- Angulo, L. (2014). *Time domain discontinuous galerkin methods for Maxwell equations*. Editorial de la Universidad de Granada, Granada.
- Balanis, C. (2012). *Advanced engineering electromagnetics*. John Wiley & Sons, Hoboken, N.J.
- Bassi, F. and Rebay, S. (1997). High-order accurate discontinuous finite element solution of the 2d euler equations. *Journal of computational physics*, 138(2):251–285.
- Baumann, D., Fumeaux, C., Vahldieck, R., and Li, E. (2008). Conformal perfectly matched absorber for finite-volume time-domain simulations. In *2008 Asia-Pacific Symposium on Electromagnetic Compatibility and 19th International Zurich Symposium on Electromagnetic Compatibility*, pages 188–191. IEEE.
- Bommaraju, C., Ackermann, W., and Weiland, T. (2009). Convergence of error in fvtd methods on tetrahedral meshes in 3d. In *2009 Applied Electromagnetics Conference (AEMC)*, pages 1–4. IEEE.
- Busch, K., Koenig, M., and Niegemann, J. (2011). Discontinuous galerkin methods in nanophotonics. *Laser & Photonics Reviews*, 5(6):773–809.

- Cai, W. and Deng, S. (2003). An upwinding embedded boundary method for maxwell's equations in media with material interfaces: 2d case. *Journal of Computational Physics*, 190(1):159–183.
- Chen, Q. and Babuška, I. (1995). Approximate optimal points for polynomial interpolation of real functions in an interval and in a triangle. *Computer Methods in Applied Mechanics and Engineering*, 128(3-4):405–417.
- Cockburn, B., Shu, C., for Computer Applications in Science, I., and Engineering (2000). *Runge-Kutta Discontinuous Galerkin Methods for Convection-dominated Problems*. ICASE report. ICASE, NASA Langley Research Center.
- Cohen, G., Ferrieres, X., and Pernet, S. (2006). A spatial high-order hexahedral discontinuous galerkin method to solve maxwell's equations in time domain. *Journal of Computational Physics*, 217(2):340–363.
- Cools, R. (1999). Monomial cubature rules since stroud a compilation part 2. *Journal of Computational and Applied Mathematics*, 112(1-2):21–27.
- Cools, R. and Rabinowitz, P. (1993). Monomial cubature rules since stroud a compilation. *Journal of Computational and Applied Mathematics*, 48(3):309–326.
- de Souza, F. E. et al. (2019). Galerkin descontínuo no domínio do tempo aplicado a problemas com múltiplas escalas em nanofotônica.
- Dey, S. and Mittra, R. (1997). A locally conformal finite-difference time-domain (fdtd) algorithm for modeling three-dimensional perfectly conducting objects. *IEEE Microwave and Guided Wave Letters*, 7(9):273–275.
- Diehl, R., Busch, K., and Niegemann, J. (2010). Comparison of low-storage runge-kutta schemes for discontinuous galerkin time-domain simulations of maxwell's equations. *Journal of Computational and Theoretical Nanoscience*, 7(8):1572–1580.
- Ditkowski, A., Dridi, K., and Hesthaven, J. S. (2001). Convergent cartesian grid methods for maxwell's equations in complex geometries. *Journal of Computational Physics*, 170(1):39–80.
- Donderici, B. and Teixeira, F. L. (2008a). Conformal perfectly matched layer for the mixed finite element time-domain method. *IEEE Transactions on Antennas and Propagation*, 56(4):1017–1026.

- Donderici, B. and Teixeira, F. L. (2008b). Mixed finite-element time-domain method for transient maxwell equations in doubly dispersive media. *IEEE transactions on microwave theory and techniques*, 56(1):113–120.
- Dumbser, M., Käser, M., and Toro, E. F. (2007). An arbitrary high-order discontinuous galerkin method for elastic waves on unstructured meshes-v. local time stepping and p-adaptivity. *Geophysical Journal International*, 171(2):695–717.
- Fahs, H. (2009a). Development of a hp-like discontinuous galerkin time-domain method on non-conforming simplicial meshes for electromagnetic wave propagation.
- Fahs, H. (2009b). High-order leap-frog based discontinuous galerkin method for the time-domain maxwell equations on non-conforming simplicial meshes.
- Fahs, H. (2010). Discontinuous galerkin method for time-domain electromagnetics on curvilinear domains. *Appl. Math. Sci*, 4(19):943–58.
- Fu, Y., Hu, X., and Gong, Q. (2013). Silicon photonic crystal all-optical logic gates. *Physics letters A*, 377(3-4):329–333.
- Fumeaux, C., Baumann, D., Leuchtman, P., and Vahldieck, R. (2004). A generalized local time-step scheme for efficient fvtd simulations in strongly inhomogeneous meshes. *IEEE Transactions on Microwave Theory and Techniques*, 52(3):1067–1076.
- Gedney, S. D. and Navsariwala, U. (1995). An unconditionally stable finite element time-domain solution of the vector wave equation. *IEEE Microwave and Guided wave letters*, 5(10):332–334.
- Georgakopoulos, S. V., Birtcher, C. R., Balanis, C. A., and Renaut, R. A. (2002). Higher-order finite-difference schemes for electromagnetic radiation, scattering, and penetration. 1. theory. *IEEE Antennas and Propagation Magazine*, 44(1):134–142.
- Golub, G. H. and Welsch, J. H. (1969). Calculation of gauss quadrature rules. *Mathematics of computation*, 23(106):221–230.
- Gordon, W. J. and Hall, C. A. (1973). Construction of curvilinear co-ordinate systems and applications to mesh generation. *International Journal for Numerical Methods in Engineering*, 7(4):461–477.
- He, B. and Teixeira, F. L. (2006). Sparse and explicit fetd via approximate inverse hodge (mass) matrix. *IEEE microwave and wireless components letters*, 16(6):348–350.

- He, B. and Teixeira, F. L. (2007). Differential forms, galerkin duality, and sparse inverse approximations in finite element solutions of maxwell equations. *IEEE Transactions on Antennas and Propagation*, 55(5):1359–1368.
- Hesthaven, J. and Warburton, T. (2004a). Discontinuous galerkin methods for the time-domain maxwell’s equations. *ACES Newsletter*, 19(ARTICLE):10–29.
- Hesthaven, J. and Warburton, T. (2007). *Nodal Discontinuous Galerkin Methods: Algorithms, Analysis, and Applications*. Texts in Applied Mathematics. Springer New York.
- Hesthaven, J. S. (1998). From electrostatics to almost optimal nodal sets for polynomial interpolation in a simplex. *SIAM Journal on Numerical Analysis*, 35(2):655–676.
- Hesthaven, J. S. and Warburton, T. (2002). Nodal high-order methods on unstructured grids: I. time-domain solution of maxwell’s equations. *Journal of Computational Physics*, 181(1):186–221.
- Hesthaven, J. S. and Warburton, T. (2004b). High-order nodal discontinuous galerkin methods for the maxwell eigenvalue problem. *Philosophical Transactions of the Royal Society of London. Series A: Mathematical, Physical and Engineering Sciences*, 362(1816):493–524.
- Hille, A., Kullock, R., Grafström, S., and Eng, L. M. (2010). Improving nano-optical simulations through curved elements implemented within the discontinuous galerkin method computational. *Journal of Computational and Theoretical Nanoscience*, 7(8):1581–1586.
- Hwang, K.-P. (2003). Computational efficiency of fang’s fourth-order fdtd schemes. *Electromagnetics*, 23(2):89–102.
- Jin (2015). *Theory and computation of electromagnetic fields*. John Wiley & Sons, Inc, Hoboken, New Jersey.
- Krivodonova, L. and Berger, M. (2006). High-order accurate implementation of solid wall boundary conditions in curved geometries. *Journal of computational physics*, 211(2):492–512.
- Lee, J.-F. (1994). Wetd/spl minus/a finite element time-domain approach for solving maxwell’s equations. *IEEE Microwave and Guided wave letters*, 4(1):11–13.

- Lee, J.-F., Lee, R., and Cangellaris, A. (1997). Time-domain finite-element methods. *IEEE transactions on antennas and propagation*, 45(3):430–442.
- Lee, J.-F. and Sacks, Z. (1995). Whitney elements time domain (wetd) methods. *IEEE Transactions on Magnetics*, 31(3):1325–1329.
- Lesaint, P. and Raviart, P.-A. (1974). On a finite element method for solving the neutron transport equation. *Publications mathématiques et informatique de Rennes*, (S4):1–40.
- LeVeque, R. J. et al. (2002). *Finite volume methods for hyperbolic problems*, volume 31. Cambridge university press.
- Luo, X., Shephard, M. S., and Remacle, J.-F. (2001). The influence of geometric approximation on the accuracy of high order methods. *Rensselaer SCOREC report*, 1.
- Lynch, D. and Paulsen, K. (1990). Time-domain integration of the maxwell equations on finite elements. *IEEE Transactions on Antennas and propagation*, 38(12):1933–1942.
- Mekis, A., Fan, S., and Joannopoulos, J. (1999). Absorbing boundary conditions for fdtd simulations of photonic crystal waveguides. *IEEE microwave and guided wave letters*, 9(12):502–504.
- Monk, P. et al. (2003). *Finite element methods for Maxwell's equations*. Oxford University Press.
- Persson, P.-O. and Strang, G. (2004). A simple mesh generator in matlab. *SIAM review*, 46(2):329–345.
- Petersen, S., Farhat, C., and Tezaur, R. (2009). A space–time discontinuous galerkin method for the solution of the wave equation in the time domain. *International journal for numerical methods in engineering*, 78(3):275–295.
- Rao, S. M. (1999). *Time domain electromagnetics*. Elsevier.
- Reed, W. H. and Hill, T. (1973). Triangularmesh methodsfor the neutrontransportequation. *Los Alamos Report LA-UR-73-479*.
- Rieben, R., Rodrigue, G., and White, D. (2005). A high order mixed vector finite element method for solving the time dependent maxwell equations on unstructured grids. *Journal of Computational Physics*, 204(2):490–519.

- Sankaran, K., Fumeaux, C., and Vahldieck, R. (2006). Cell-centered finite-volume-based perfectly matched layer for time-domain maxwell system. *IEEE transactions on microwave theory and techniques*, 54(3):1269–1276.
- Sármány, D., Botchev, M. A., and van der Vegt, J. J. (2007). Dispersion and dissipation error in high-order runge-kutta discontinuous galerkin discretisations of the maxwell equations. *Journal of Scientific Computing*, 33(1):47–74.
- Sarris, C. D. (2007). Adaptive mesh refinement for time-domain numerical electromagnetics. *Synthesis Lectures on Computational Electromagnetics*, 1(1):1–154.
- Shewchuk, J. R. (1996). Triangle: Engineering a 2d quality mesh generator and delaunay triangulator. In *Workshop on Applied Computational Geometry*, pages 203–222. Springer.
- Shu, C.-W. (2009). Discontinuous galerkin methods: general approach and stability. *Numerical solutions of partial differential equations*, 201.
- Silveira, A., Moura, R., Silva, A., and Ortega, M. (2015). Higher-order surface treatment for discontinuous galerkin methods with applications to aerodynamics. *International Journal for Numerical Methods in Fluids*, 79(7):323–342.
- Stroud, A. H. (1971). Approximate calculation of multiple integrals.
- Tang, C. C. (1957). Backscattering from dielectric-coated infinite cylindrical obstacles. *Journal of Applied Physics*, 28(5):628–633.
- Taylor, M. A., Wingate, B. A., and Vincent, R. E. (2000). An algorithm for computing fekete points in the triangle. *SIAM Journal on Numerical Analysis*, 38(5):1707–1720.
- Van der Vegt, J. J. and Ven, H. (2001). Space-time discontinuous galerkin finite element method with dynamic grid motion for inviscid compressible flows.
- Wandzurat, S. and Xiao, H. (2003). Symmetric quadrature rules on a triangle. *Computers & Mathematics with Applications*, 45(12):1829–1840.
- Williamson, J. (1980). Low-storage runge-kutta schemes. *Journal of Computational Physics*, 35(1):48–56.
- Xu, Y. and Shu, C.-W. (2005). Local discontinuous galerkin methods for nonlinear schrödinger equations. *Journal of Computational Physics*, 205(1):72–97.



- Yee, K. (1966). Numerical solution of initial boundary value problems involving maxwell's equations in isotropic media. *IEEE Transactions on antennas and propagation*, 14(3):302–307.
- Young, J. L. (2001). High-order, leapfrog methodology for the temporally dependent maxwell's equations. *Radio Science*, 36(1):9–17.
- Zhang, X. (2016). A curved boundary treatment for discontinuous galerkin schemes solving time dependent problems. *Journal of Computational Physics*, 308:153–170.